DrEngMuslim - Karya Ilmiah - Application Of Polymeric Nanofluid In Enhancing Oil Recovery At Reservoir Condition

by Drengmuslim Karya Ilmiah

Submission date: 19-Aug-2022 08:13AM (UTC+0700)
Submission ID: 1884148493
File name: c_nanofluid_in_enhancing_oil_recovery_at_reservoir_condition.pdf (5.73M)
Word count: 13817
Character count: 73110

Journal of Petroleum Science and Engineering 194 (2020) 107476

Contents lists available at ScienceDirect

Journal of Petroleum Science and Engineering

journal homepage: http://www.elsevier.com/locate/petrol

Application of polymeric nanofluid in enhancing oil recovery at reservoir condition

Augustine Agi [a], Radzuan Junin [a,b,*], Mohammed Omar Abdullah [c], Mohd Zaidi Jaafar [a], Agus Arsad [b], Wan Rosli Wan Sulaiman [a], M.N.A. Mohd Norddin [a], Muslim Abdurrahman [d], Azza Abbas [a,e], Afeez Gbadamosi [a], Nur Bashirah Azli [a]

[a] Department of Petroleum Engineering, School of Chemical and Energy Engineering, Faculty of Engineering, Universiti Teknologi Malaysia, 81310, Johor Bahru, Malaysia
[b] Institute for Oil and Gas, Universiti Teknologi Malaysia, 81310, Johor Bahru, Malaysia
[c] Department of Chemical Engineering and Energy Sustainability, Faculty of Engineering, Universiti Malaysia Sarawak, Kota Samarahan, Sarawak, Malaysia
[d] Department of Petroleum Engineering, Universitas Islam Riau, Jl. Kaharudin Nasution, No. 113 KM 11, Perhentian Marpoyan, Pekanbaru, 28284, Riau, Indonesia
[e] School of Computing, Engineering and Technology, Asia Pacific University of Technology & Innovation (APU), 57000, Kuala Lumpur, Malaysia

ARTICLE INFO

Keywords:
EOR
Cissus populnea
IFT
Wettability
Ultrasound
Nanofluid

ABSTRACT

In this study, ascorbic acid was used to synthesize *Cissus populnea* nanoparticles (CPNP). The synthesized CPNP was isolated and the influence of the process variables on the physical properties were studied. The rheology of the formulated *Cissus populnea* nanofluid (CPNF) was measured and compared with *Cissus populnea* (CP) solution and commercial polymer xanthan. Moreover, the interfacial properties of CPNF were studied at various concentrations and temperatures, and the influence of salinity and their interaction with ultrasound was investigated. Sessile drop contact angle method was used to determine the wettability alteration efficiency of CPNF on an initially oil-wet sandstone core surface. Finally, CPNF and CP solutions were evaluated for EOR purposes at typical reservoir condition. The displacement process was scaled to reduce the number of parameters investigated using dimensionless parameters. The synthesis methods were efficient in generating sphere-shaped and elongated nanoparticles (50 nm mean diameter). Experimental results show that an increase in temperature of CP and CPNP yielded increased viscosity of the solutions in stark contrast to xanthan whose solution viscosity declines as the temperature increases. Besides, the CPNF was effective in lowering IFT at oil-water (O/W) interface and altered the wettability of the sandstone cores to water-wetting condition. The novel CPNF increased the oil recovery by 26% and was effective at high-temperature high-pressure (HTHP) reservoir condition. The result shows a transition from capillary dominated flow to gravity dominated flow as decrease in IFT decreased residual oil saturation and increased capillary and Bond number. The energy consumption and cost estimation of the proposed novel polymeric nanofluid shows it is cost-effective than conventional EOR chemicals.

1. Introduction

Recently, the oil and gas industries are grappling with the reality of scarcity of new sizeable or commercial discoveries and low production from existing reservoirs. Significant amount of oil remains in the reservoir after the primary and secondary recovery methods due to capillary trapping and heterogeneity of reservoirs (Gbadamosi et al., 2018). To recover the remaining oil, enhanced oil recovery (EOR) methods are the only viable option which can reduce the gap between demand and supply. Since the exploration of new fields requires huge amount of capital, EOR processes are used to improve the productivity of the fields which aims to recover the oil left in the reservoirs after the primary and secondary oil recovery methods.

To overcome the low oil sweep efficiency, numerous EOR methods such as gas, chemical, and thermal, have been devised and utilized (Gbadamosi et al., 2019a). Amongst all the EOR techniques, chemical EOR (CEOR) method has been adjudged as the most promising because of its higher efficiency, reasonable capital cost, technical and economic

* Corresponding author. Department of Petroleum Engineering, School of Chemical and Energy Engineering, Faculty of Engineering, Universiti Teknologi Malaysia, 81310, Johor Bahru, Malaysia.
E-mail address: r-radzuan@utm.my (R. Junin).

https://doi.org/10.1016/j.petrol.2020.107476
Received 22 October 2019; Received in revised form 29 May 2020; Accepted 29 May 2020
Available online 5 June 2020

feasibilities. CEOR methods are effective in increasing oil recovery. CEOR chemicals can alter fluid-fluid and/or fluid-rock interaction in the reservoir by reducing interfacial tension (IFT) between the imbibing fluid and oil and/or increase the viscosity of the injected fluid for mobility control. The injected chemicals can also alter wettability of the rock to increase oil permeability (Zhou et al., 2015a, 2018a; Abbas et al., 2020).

Polymer flooding, surfactant and/or alkaline flooding are the conventional EOR methods (Gbadamosi et al., 2020). Recently, the use of foam enriched by surfactants or polymers for mobility control have been studied and found to be effective in improving oil recovery (Zhou et al., 2015b, 2018b). Field practices have shown that polymer flooding can increase oil recovery up to 5–30% original oil initially in-place (OOIP) (Pope, 2011). Hydrolysed polyacrylamide (HPAM) are widely used in polymer flooding because of inexpensive handling cost, relatively resistant to bacterial attack, high solubility in water and high ability to reduce permeability of water (Gbadamosi et al., 2019b, c). However, with variation in reservoir conditions (high temperature, pressure and salinity) and crude oil properties, existing chemical flooding materials used in CEOR, such as polymers and surfactants do not function desirably. These conditions have detrimental effect on the performance of EOR chemicals, such as degradation and precipitation. Therefore, various studies are being carried out to improve the limitation of polymer such as HPAM against high temperature and high salinity reservoir conditions. More recently, researchers have reported the use of nanofluid in CEOR process. Nanofluid which is the synergy of base fluid with nanoparticles has the advantages of being more tolerant to high salinity, high temperature, longer stability, less plugging and retention in highly permeable reservoir (Zhou et al., 2017). Nevertheless, despite the sterling results reported in earlier works, concerns have been raised on the cost of the full-scale field implementation and toxicity of the nanofluids (Agi et al., 2018a). As the oil and gas industry continue to deal with the reality of scarcity of new sizeable or commercial discoveries and low production from existing reservoirs, it is essential that low-cost and environmental friendly nanoparticles obtained from organic source are considered (Agi et al., 2018b).

Cissus populnea (CP) is one of the most abundant biopolymers found mostly in the tropics and used as a renewable raw material in a wide range of applications (Bouatay et al., 2014; Oladimeji and Okechukwu, 2016). It has close resemblance to xanthan gum used in confectionary and oil industry. The choice of this biopolymer as a starting raw material is because it contains cellulose, starch and fibres which are known to have rigid and long polysaccharide chain that is stable at high temperature condition (Agi et al., 2018b). It is an in-expensive and non-toxic biopolymer which makes it attractive for industrial applications (Mo[illegible]n et al., 2011).

The main approach adopted to produce biopolymer nanoparticles is acid hydrolysis (Chin et al., 2011; Bel Haaj et al., 2013). This approach is effective in producing small size nanoparticles (5–7 nm) but has its limitations. These include long duration of synthesis and low yield of the nanoparticles (LeCorre et al., 2010; Shahrodin et al., 2015). Also, nanoparticles obtained by classic acid tends to aggregate in powder form and are limited for industrialized utilization (Dufresne, 2008). Ultrasound have been proven to be a very effective method of synthesizing biopolymers (Suslick, 2001). Ultrasonic treatment of biopolymers can reduce molar mass of the biopolymer, reduce the synthesis time and prevent aggregation (Agi et al., 2019a). Although, Kim et al. (2013) and Goncalves et al. (2014) stated that ultrasonic can reduce the crystallinity of nanoparticles, contrariwise, ultrasonic can also improve the crystallinity of the synthesized nanoparticles by intensifying the process (Kim et al., 2013; Agi et al., 2019a). Preservation of crystallinity after synthesis will improve the industrial applicability of the nanoparticles (Kim et al., 2013; Goncalves et al., 2014).

Nanofluid application in EOR has recorded a lot of success and the performance is based on the material used and preparation method. Earlier works on synthesis of biopolymers used classic acid (HCl and H_2SO_4) but this method has recorded low yield. The combination of acid hydrolysis with ultrasonic has resulted in loss of crystallinity. However, the use of ascorbic acid, process intensification and homogenization were not considered. The use of inorganic and metal oxide nanofluids in EOR has been thoroughly investigated. However, the use nanoparticles from natural and/or organic source have not been considered.

Hence, in this study, a combined methods of ascorbic acid hydrolysis, ultrasound and nanoprecipitation were utilized for the first time to produce *Cissus populnea* nanoparticles (CPNP). Isolation and influence of the process variables on physical properties of CPNP were studied. Rheology of *Cissus populnea* nanofluid (CPNF) was compared with CP and xanthan solutions. Besides, the interfacial properties of CPNF were studied at various concentration and temperatures. Additionally, the effect of concentration, temperature, electrolyte and their interaction with ultrasound on the synthesized CPNF were determined. Sessile drop contact angle method was used to determine wettability effectiveness of CPNF on an initially oil-wet sandstone core. Finally, CPNF and CP solutions were evaluated for EOR purposes at typical reservoir condition. The displacement process was scaled to reduce the number of parameters investigated using dimensionless parameters. The energy and cost estimation of the methods and materials were determined and compared with conventional methods.

2. Materials and methods

2.1. Materials

CP was harvested from a local farm in Nigeria. The fruits (oranges and pineapples) were purchased from a grocery shop in Johor Bahru, Malaysia. Lemongrass was handpicked from Universiti Teknologi Malaysia (UTM) campus orchard. Palm wine, which acted as the alcohol and surfactant, was purchased from Kangkar Pulai, Johor and has a purity of 94%. Xanthan gum was purchased from R&M Marketing, Essex, U.K. Sodium chloride (NaCl) with molecular weight of 58.44 g/mol and a purity of 99% assay was purchased from QREC (ASIA) Sdn. Bhd., Selangor, Malaysia. Vinegar was purchased from PubChem, it has a molecular weight of 60.05 g/mol, acetic acid (5%) and density of 1.0446 g/mL @ 25 °C. Toluene with a molecular weight of 92.14 g/mol was supplied by PubChem. Crude oil sample (West Lutong) with density of 0.8283 g/mL @25 °C, API gravity 37.7 and viscosity of 10 mPa s @25 °C was obtained from an oil field in Sarawak, Malaysia. The oil was centrifuged to remove emulsified oil. Core samples from a sandstone formation located in Sarawak, Malaysia were used to simulate the reservoir condition of a typical reservoir rock of Sarawak oil field. Table 1 shows the properties of the core samples.

2.2. Methods

2.2.1. CPNP production

CP was prepared to dry powder form using the method described in previous study (Agi et al., 2019b). The dried CP was soak in 1 L of distilled water (DW) for 20 min to generate exudes. Vinegar (20 mL) was used to disperse the exudes to form a solution and subsequently added in drops to the alcohol. Ascorbic acid was extracted from pineapple,

Table 1
Properties of core samples.

Properties	Core #1	Core #2	Core #3
Length (cm)	9.7	9.8	9.9
Diameter (cm)	3.7	3.7	3.7
Bulk Volume (cm^3)	104.30	105.37	106.45
Pore Volume (cm^3)	16.00	16.00	16.00
Porosity (%)	15.3	15.2	15.0
Permeability (mD)	167.43	152.24	102.53
Initial Oil Saturation (%)	98.13	93.44	95.00
Injection rate (mL/min)	0.5	0.5	0.5

oranges and lemongrass as reported elsewhere (Agi et al., 2019b). It was added gradually to the solution at a ratio of 1:10 (v/v). A magnetic stirrer was used to agitate the mixture at a constant rate, temperature (60 °C) for 120 h. The mix was then sonicated for 3 h. The dimension of the ultrasonic bath and properties of ultrasonic generator has been reported elsewhere (Agi et al., 2018c). Centrifugation was used to isolate the nanoparticles. Thereafter, the obtained nanoparticles were washed three times and air dried. The energy used for the synthesis process was calculated using equation (1).

$$E = \frac{Pt}{R_m} \quad (1)$$

whereas E is energy used (J/g), P is power applied (J/s), t is ultrasonic time, R_m is quantity of treated raw material (g). The synthesis schematic route is shown in Fig. 1.

2.2.2. Morphology

A Zeiss (LEO) 1450VP scanning electron microscope (SEM), Germany and Oxford instrumentation INCA software, UK, was used to determine the structure and size of the CP. The samples were sputter-coated with gold to provide a conductive coating. The imaging was achieved at an electrical energy of 13 kV and 500× magnification. Sizes of CPNP were obtained utilizing transmission electron microscopy (TEM) HITACHI (HT 7700) image analyser. The samples were prepared by dispersing in distilled water (DW) and positioned on a platinum-coated microscopy grid. The samples were captured at an electrical energy of 120 kV. An inbuilt HITACHI EMIP-SP electron microscope image integration software automatically measured the particles sizes and enhanced the images.

2.2.3. Particles size analysis and surface charge

A litesizer™ 500 Anton Paar equipment was used to determine the particle size distribution and zeta potential. CP and CPNP were dissolved in DW (0.1%) and moved to omega cuvette for measurement. The measurement was carried out at a fixed back scattering angle of 170° at 25 °C. The refractive index of water was 1.3303 and the viscosity of water was 0.8903 mPa s.

2.2.4. Carbon nuclear magnetic resonance (^{13}C-NMR)

The ^{13}C-NMR spectra experiments were carried out using Bruker Advance II 400 MHz spectrometer. The spectra were recorded at width of 100.6 MHz and placed between 30 and 110 ppm. A recycle delay of 2 s was applied with a contact time of 1.2 s.

2.2.5. Preparation of CPNP, CP and xanthan solutions

CPNP, CP and xanthan at different concentrations (750–2000 ppm) were dissolved in deionized water (DIW). The dispersion was agitated for 2 h and sonicated for 25 min to form a stable solution. The same concentration (2000 ppm) of the solutions were prepared in different NaCl solutions (0.9 wt% - 2.2 wt%) to investigate the effect of salinity. This range of salinity was selected to represent a normal Malay Basin and Sarawak Basin oilfields salinity (Agi et al., 2019c).

2.2.6. Viscosity measurement

A 350 RST BROOKFIELD rheometer was used determine the rheology of the CPNF, CP and xanthan solutions. The rheometer was equipped with temperature controller and a water bath connected to the rheometer for high temperature measurement. The samples were transferred into a holder at the desired temperature. The steady shear data were obtained at a shear rate ranges of 1–1000 s^{-1} at different temperatures 26–80 °C.

2.2.7. IFT measurement

The IFT was measured using KRUSS EasyDyne K20 tensiometer. The ring technique was applied to determine IFT of CPNF at various concentrations (0.05–0.2 wt%) as a function of NaCl concentrations (0.9–2.2 wt%) and temperature (26–80 °C). The measurement was based on the fact that for any enlargement of a phase boundary area

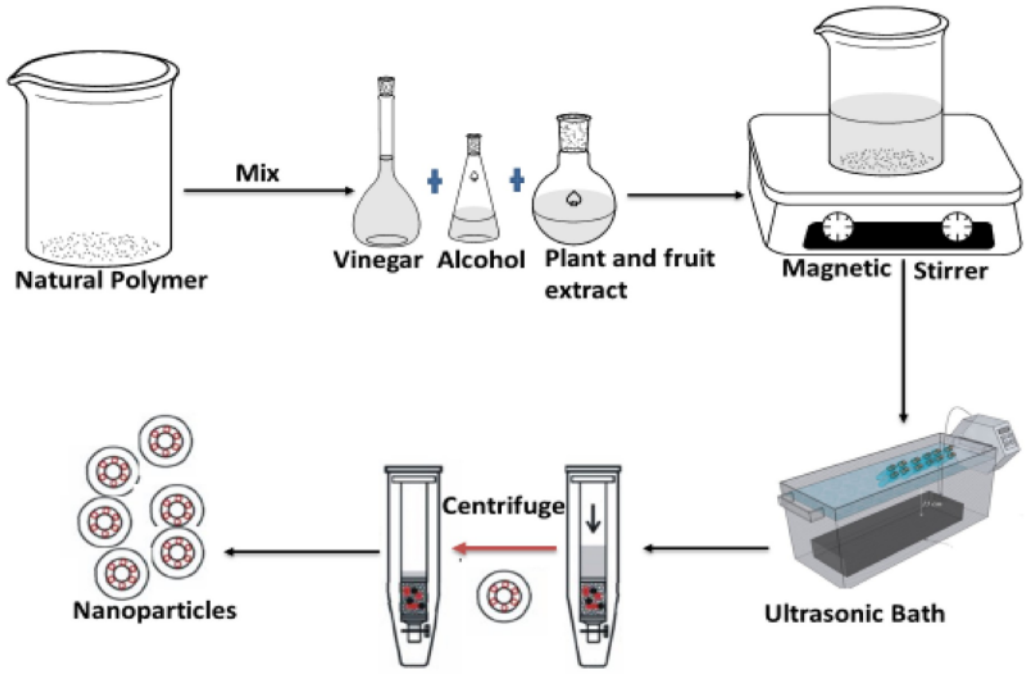

Fig. 1. Synthesis schematic route for CPNP.

between liquid/air or liquid/liquid to occur, some resistance has to be overcome. This resistance was proportional to existing surface and IFT. The result was directly read in mN/m with an accuracy of ±0.1 mN/m and high sensitivity.

2.2.8. Sample preparation and contact angle measurement

The sessile drop technique was used to measure angles of contact at different conditions of wettability. Sixteen sandstone cores with flat surface (1 cm thick x 5 cm diameter) were used to measure the contact angles. The sandstone surfaces were flushed with clean air to remove any loose sand. Subsequently, it was cleaned with DW and toluene to remove any organic matter and air-dried for 24 h. The cleaned sandstone cores were made oil-wet by placing in a small glass beaker and crude oil was pipetted gradually on the sample surface until it was fully immersed in crude oil. The beaker was sealed to prevent evaporation and contamination, and then placed in the oven for 78 h at 90 °C. To prepare the samples for wettability assessment, the samples were washed with n-heptane and DW making it oil-wet, and afterwards air-dried for 24 h. To test wettability alteration efficiency of the CPNF, the induced oil-wet sandstone cores were submerged in a previously prepared CPNF of various concentrations for 76 h and dried for 22 h. Wettability assessment of the sandstone core before and after treatment with CPNF was performed by estimating the contact angles. This was done by placing an oil drop (0.1 cm^3) on a horizontally held sandstone core using a U-shaped needle. The image of the drops at 26 °C - 80 °C were captured using Nikon P900 microscopic digital camera. An Image J 1.48s image analyser software was used to estimate the contact angle. Schematic representation of the experimental process is presented in Fig. 2.

2.2.9. Core flooding test

The displacement test was investigated using reservoir sandstone core with the equipment shown in Fig. 3. The flooding apparatus is a high temperature high pressure (HTHP) equipment manufactured by Fars EOR technologies. It was designed for determining oil recovery for different injection fluids. It has a maximum pressure capacity of 6000 psi and temperature limit of 150 °C. The equipment is equipped with an oven for regulating the temperature, four compartments for holding the injection fluids and a core holder for performing different injection scenes. Three core samples from the same location as that used for the wettability test were utilized for the flooding (Table 1). The cores were cleaned with toluene in a Soxhlet distillation extraction column after each use and dried in an oven for 48 h at 100 °C. Core flooding experiments were performed to determine the oil displacement performance of CPNF and CP solutions in comparison with xanthan solution. The unit was pressured up to 3000 psi supported with a back pressure of 100 psi. The oven temperature was increased to 120 °C to mimic reservoir condition of a Sarawak oil field. The equipment was air vacuumed, saturated with synthetic brine (2.2 wt%) and flooded with oil until connate water saturation was achieved. The injectants from the accumulator were pumped through the core flooding system using ISCO displacement pump. Crude oil was injected into the core at a flow rate of 0.5 mL/min and allowed to age for 24 h to attain equilibrium. Thereafter, water was injected at the same flow rate (0.5 mL/min) until breakthrough (BT) occurred. Afterwards, 0.5 PV comprising 0.2 wt% (CPNF, CP, and xanthan solutions) was injected to retrieve the bypassed oil. Chase water (0.5 PV) was injected to evaluate the total recovery. All the experiments were conducted in triplicate and the average reported.

2.2.10. Dimensionless parameter theory

Capillary, viscous, hydrodynamic and gravity forces controls the flow of fluid in porous media. The relationship (ratio) between these controlling forces is expressed as a dimensionless number (Agi et al., 2018c, 2019d). Dimensionless parameters can be utilized in understanding influence of the major forces in EOR process. Hydrostatic equilibrium determines the microscopic circulation of O/W and this microscopic displacement process is controlled by capillary forces. To evaluate the transition between a capillary and viscous dominated displacement process, it will be appropriate to think of the dependence of oil recovery on a suitable dimensionless parameter like capillary number (N_c) and Bond number (N_B):

$$N_C = \frac{\mu\nu}{\sigma} \tag{2}$$

$$N_B = \frac{\Delta P_{grav}}{\Delta P_{cap}} = \frac{\Delta\rho g k/\phi}{\sigma} \tag{3}$$

whereas μ is viscosity of fluid (mPa.s), ν is velocity of fluid (m^3/s) and σ is O/W IFT (mN/m), $\Delta\rho$is density difference between two fluids (g/mL), g is acceleration due to gravity (m/s^2), k and ϕ are permeability (mD) and porosity (%) of the porous medium respectively. Dimensionless parameters allow scaling from field condition to laboratory condition, this enables the laboratory experiments to be reproduceable with the same forces as those in the field (Agi et al., 2018c).

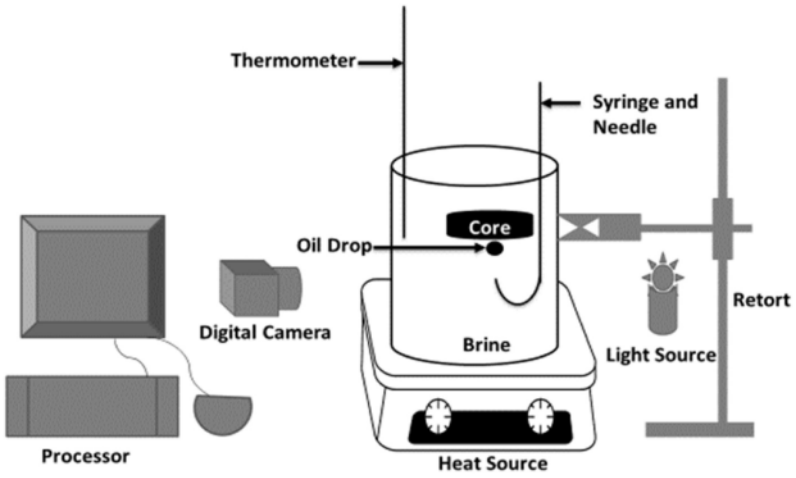

Fig. 2. Schematic representation of contact angle experiment.

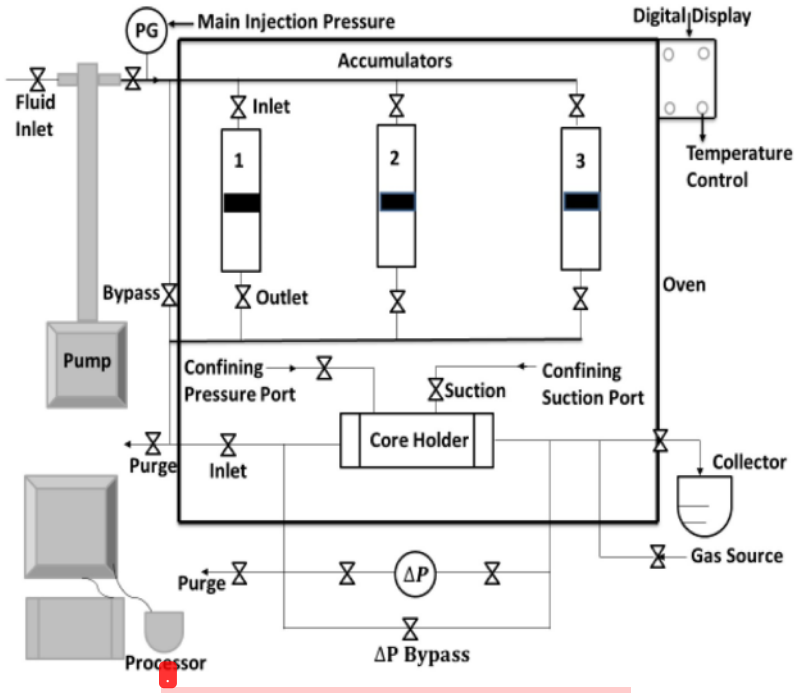

Fig. 3. Schematics of the core-flooding experimental apparatus.

3. Results and discussion

3.1. Morphology and structural change

Morphological analysis of CP was carried out using SEM. It provides visual evidence for the formation of multilayer interfaces around the particles. The biological source of these natural polymers most often determines their granular shape, size and morphology. The CP exhibited elongated-oval shape (Fig. 4a) with flaky-mucilage of the gum (indicated with red circles) resting on top of the granules. The flaky mucilage (Fig. 4b) shows irregularly shaped network structure indicating the involvement of the inter and intramolecular aggregation of the particles (Luzi et al., 2014; Deshmukh and Aminabhavi, 2015). The particles range from 1 to 10 μm. Fig. 5 shows energy dispersive X-ray (EDX) spectra, the major elements are carbon (C) and oxygen (O) while potassium (K) appears as a minor element. The strong signal appears at 0.1–0.6 keV whereas the weak peak appears at 3.3–3.6 keV in the EDX spectra (Fig. 5). The atomic percentage (Table 2) was close to the

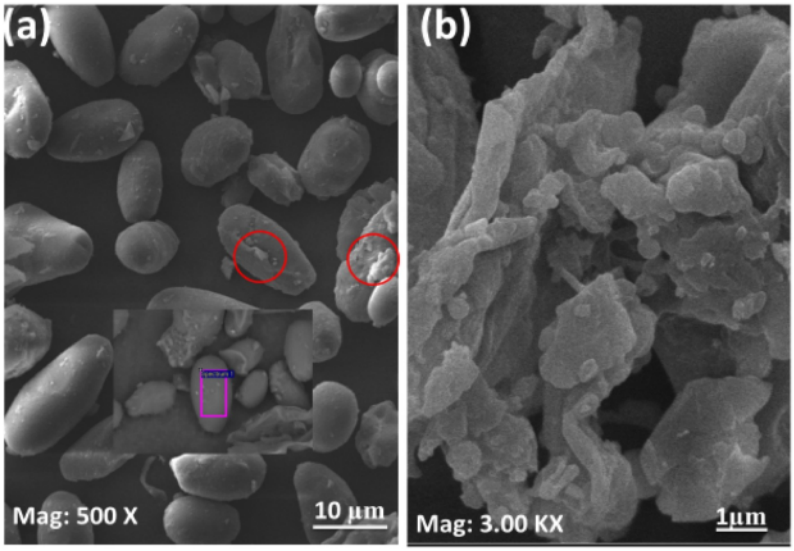

Fig. 4. SEM image of CP (a) showing elongated-oval shape, and (b) flaky exudes of the gum.

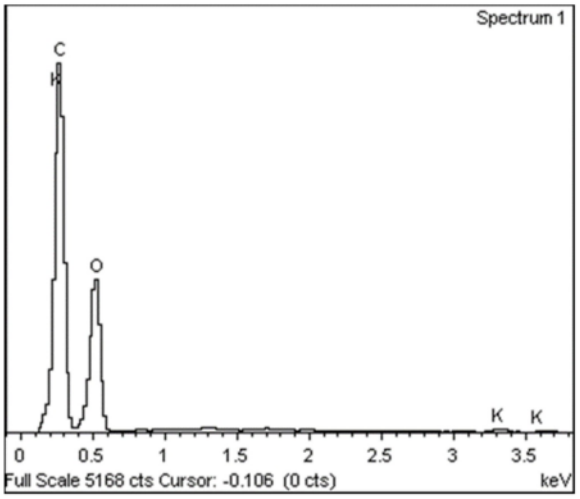

Fig. 5. EDX spectra of CP.

Table 2
CP EDX data.

Elements	Weight (%)	Atomic (%)
C	52.75	60.01
O	46.51	39.73
K	0.73	0.26
Total	100	100

stoichiometry 1: 2: 59 ratios for C: O: K, respectively. The EDX analysis demonstrates that the oval clusters on the surface are mainly composed of C and O and shows that their origin are from plant. The elemental percentage depends on the chemical structure of the material extracted.

Fig. 6 shows the TEM image of CPNP at different magnification, it discloses that the particles are well distributed with particle ranging from 7.45 to 29.3 nm (Fig. 6a). Large amount of small (7.45–10.1 nm) poly-dispersed particles were formed (Fig. 6b), larger particles (15.9–29.3 nm) were also produced (Fig. 6a). This is probably due to the diffusion of smaller particles to the side of the medium, which resulted to aggregation and subsequently increase in size (Guidelli et al., 2011). The size increase was confirmed when the magnification in that region was increased (Fig. 6a), which depicts that the agglomeration was caused by smaller particles. The shape of the nanoparticles varied from spherical, hexagonal and rod-like, which is consistent with the SEM results (Fig. 4). At the early stage of nanoparticles formation process, nanoparticles growing through coagulation snowballed into spherical particles because of the temperature near the source of the material during synthesis (Ku and Maynard, 2005). This is because the heating system with a localized area has a thin area with a high temperature on the surface, the generated nanoparticles may grow spherically. The combination of thermophoretic force, a positive unipolar electric force and diffusion mixing by the local temperature contributed to the formation of non-agglomerated spherical nanoparticles (Ku and Maynard, 2005; Zhou et al., 2019a, b). As the coagulation between the particles decrease rapidly due to quenching effect and dilution effect, the particles move from spherical shape to other forms such as hexagonal and rod-like as noticed in Fig. 6a.

3.2. Mechanism of nanoparticle synthesis

The chlorogenic acid present in the plant and fruit extract acted as a stabilizing agent and synergistically reducing the microparticles to nanoparticles (Scott et al., 1993). The antioxidant and free scavenging abilities of the plant and fruit extract are attributed to the orthodihydroxl and ortho-diphenolic functional group in the catechol ring of the compound. These functional groups can act as H-atom donor towards reactive oxygen species and other biological oxidants. This enabled the sample subjected to weak-acid hydrolysis to have more homogenous size (Fig. 6c). Ultrasonic enhanced the chemical reaction initiated and decreased the diffusion layer thickness initiated by the plant and fruit extracts. Free radicals were produced during acoustic cavitation, which involves the formation, growths and collapse of bubbles. The violent collapse of these cavitation bubbles (indicated with red circle in Fig. 6d) generated high pressure which might have initiated nucleation (Suslick et al., 2018). Ultrasonic cavitation also improved the rate of heat and mass transfer resulting to nanoparticles clusters. These clusters become bigger than the critical nucleus which might have resulted in CPNP growth (Fig. 6a). The vinegar broke down the hydrogen bond of the CP and prevented self-association which enhanced solubility (Chin et al., 2011). The addition of alcohol led to precipitation of the CPNP which affected the morphology. The fibrous shape (Fig. 6b) is consistent with previous study of Chin et al. (2011) when a ratio of 1:10 (v/v) of ethanol was used.

3.3. Particles size distribution and stability

Fig. 7a shows the size distribution of CP, with a mean particle size (D_{50}) of 7.8 μm (Table 3). The small sizes of the particles show the ability of the particles to deform and shows the ability of the particles to emulsify, viscosify and stabilize materials which might have influence on the rheology behaviour of the CP (Yildirim et al., 2016). Also, the small particle size could have been attributed to cause increase stability. The small particles are separated at lower velocities due to gravitational forces (Okachi and Nakano, 2000; Cofrades et al., 2013). Besides, the smaller particles decrease the movement of droplets, inhibit sedimentation and other instabilities (Yildirim et al., 2016).

Fig. 7b displays the particle size distribution for CPNP. The sample is polydisperse with a PDI of 0.27. Polydisperse suspensions contain particles of different sizes forming a broad distribution (Baalousha and Lead, 2013). The CPNP shows two peak intensity which agrees with the TEM results (Fig. 6) and confirms the formation of nanoparticles. The result agrees with earlier work of Guidelli et al. (2011). They stated that diameters obtained by DLS are of equal magnitude as those of agglomerate as revealed by TEM micrograph. It shows that DLS results are linked to larger state of clusters of nanoparticles (Guidelli et al., 2011). This was observed in the mean peak intensity at 952.1 nm (Table 4), which was larger than the size obtained from TEM (Fig. 6). Another possible explanation could be because of water retention by CP, which could result to swelling of the nanoparticles and consequently increase in size (Guidelli et al., 2011). Thus, the light scattering of large particles increased which might have influence the intensity of the DLS results. Therefore, DLS measures the hydrodynamic size of the hypothetical hard sphere that diffuses similarly to the particles being measured (Zetasizer Nano Series User Manual, 2015). Hence, the diameter estimated from the diffusion properties of the CPNP are only indicative of the apparent size of the dynamic hydrated/solvated particles. It does not reflect the actual size for non-monodispersed and non-spherical samples. Thus, despite the fractionation, the measurement remains complex (LeCorre et al., 2011). Consequently, the hydrodynamic diameter reported cannot be used as an approximation of size but rather for comparison (LeCorre et al., 2011).

Zeta potential is a useful tool in material science when studying the stability of materials. The zeta potential of CP is illustrated in Fig. 8a. The result shows a mean zeta potential of −20.3 mV (Table 5). The negative charge of the CP was due to the presence of free carboxylic group (Brar and Kaur, 2018). In a colloidal system such as this, the charges arise from either the ionization and/or dissociation of the surface groups, differential ion adsorption of the active surface, the

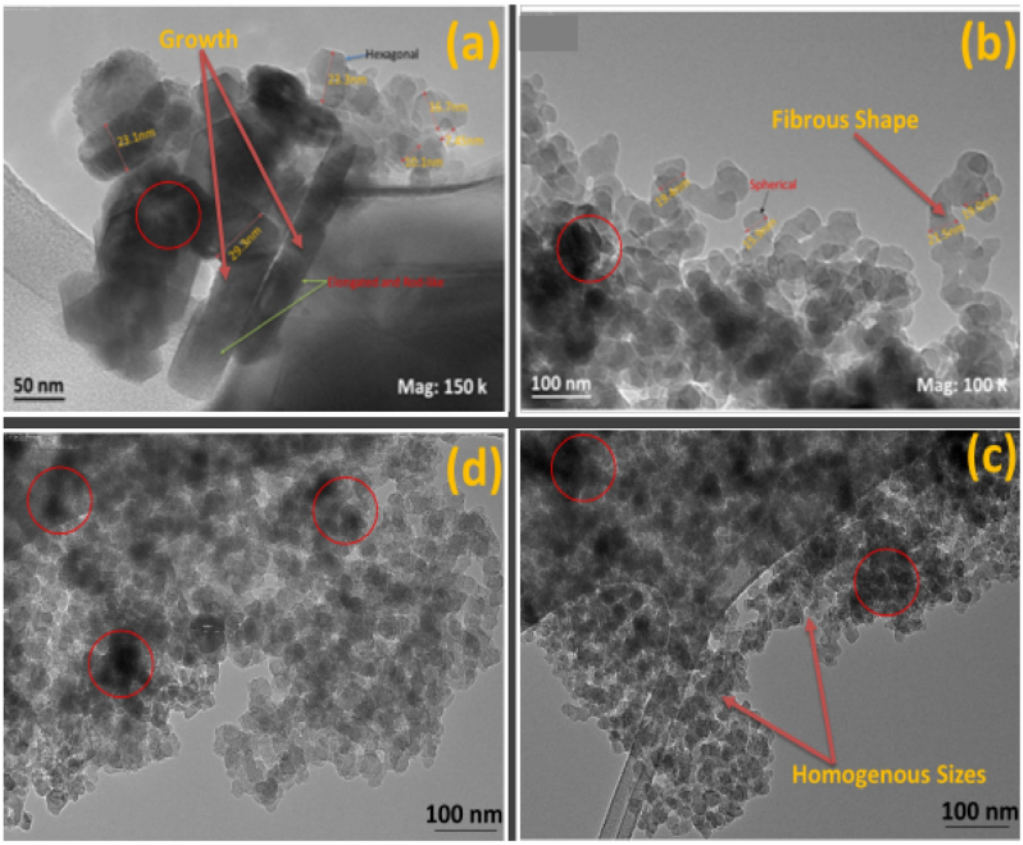

Fig. 6. TEM image of CPNP (a) rod-like shape due to growth (b) fibrous shape (c) homogenous size particles (d) nucleation due to cavitation bubbles.

continuous charges related to the crystalline lattice or all of these mechanisms (Zasoski, 2008; Cano-Sarmiento et al., 2018). The result indicates that CP is discreetly stable, and it can produce good interaction with other materials used in EOR. This agree with previous study by Kalesi et al. (2016) when they examined the interaction between Persian gum and whey protein isolate at pH of 7. The zeta potential aided in proving the existence of interaction between the two negatively charged biopolymers, which shows that the Persian gum and the whey protein isolate can interact effectively.

Zeta potential has also been linked to the increment or decrease of CPNP peptide bond (David-Birman et al., 2013). Fig. 8b shows the zeta potential of CPNP to be −25.1 mV (Table 6). The high stability of CPNP and their ability to hold hydrophilic and hydrophobic compounds makes them excellent delivery medium in porous media (Chuah et al., 2009; Goyal et al., 2016; Cano-Sarmiento et al., 2018). The dominant mechanism is the adsorption of the active surface of CPNP which might have influenced the zeta potential by (i) influencing the adsorption characteristics of the ions present, and (ii) shifting the position of the plane of shear from the particle surface.

3.4. ^{13}C-NMR spectra of CP and CPNP

^{13}C-NMR was used to identify the chemical structure and composition by solution state high resolution of CP (Fig. 9a) and CPNP (Fig. 9b). The resonance at 60.89 ppm was assigned to C-6, the signal around 72.07–73.7 ppm was collectively associated with C-2, C-3 and C-5 sites. The resonance at 79.18 ppm was associated with C-4 site and the resonance at 100.5 ppm was associated with C-1 site. Both spectra showed remarkable similarities which shows that they are from the same source. The major differences in the pattern was the disappearance of the peak in the CPNP (Fig. 9b), which shows the conversion of the CPNP to B-crystallinity from the original A-crystallinity of the CP. This implies that the appearance of the peak was directly proportional to the CP content. Moreover, the intensity of the resonance increased for the CPNP compared to the CP (Table 7). This indicates that the content of the amylose-lipid complex was higher in the CPNP compared to the CP (Wei et al., 2010).

3.5. Rheological behaviour of CP as a function of concentration

Rheological profile of CP solution at 26 °C is shown in Fig. 10. At all the concentrations, the apparent viscosity of CP declined with increase in shear rate, thus, displaying a non-Newtonian, shear-thinning behavior (Alakali et al., 2009). The shear-thinning behavior was a result of the structural deformation of the network structure of the CP. This flow behavior was because of the collapse of the structural unit of CP and the reordering of its particles in the path of hydrodynamic forces produced during the shear. This resulted in a lesser communication among the adjoining particles of the CP, resulting to reduction in viscosity (Hosseini et al., 2017). Similar result was reported by Awonorin (1993) when he observed that this phenomenon is common with hydrocolloids with sensitive structures. On the other hand, viscosity of the solution increased as concentration increases. The interaction of the molecules resulted in more viscous liquid. This is of interest in the formulation of suspensions where resistance to shear of agitation may impair easy flow in porous media. The shear-thinning region was fitted with Ostward

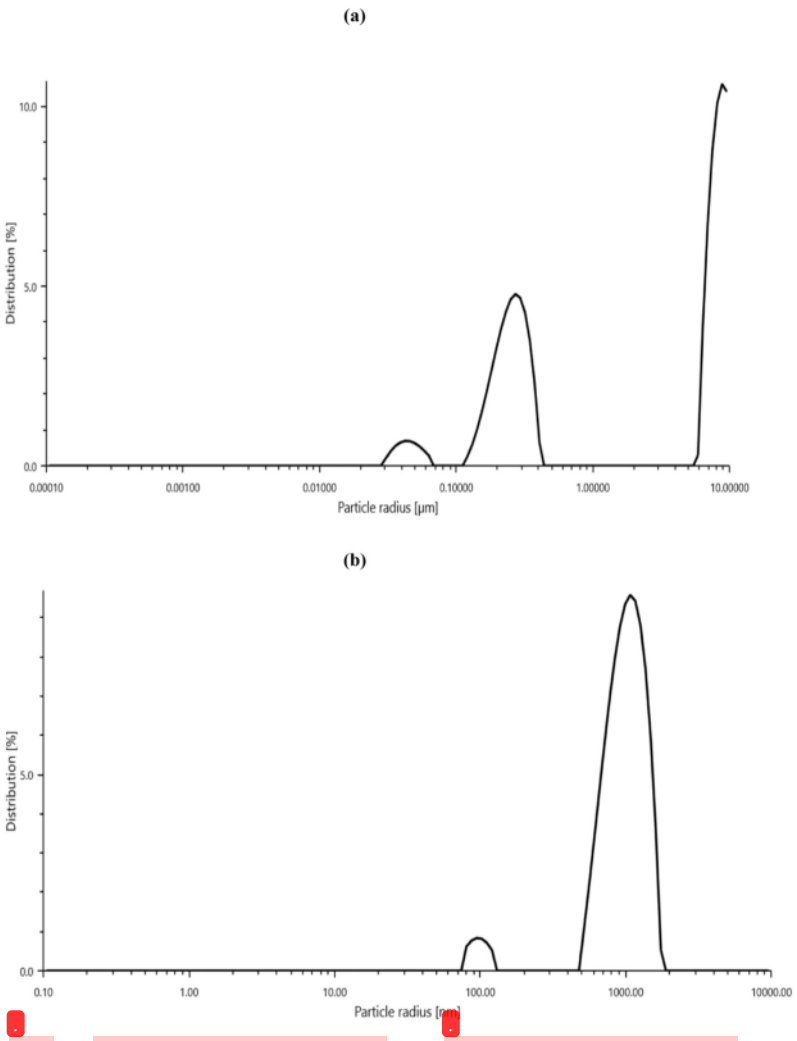

Fig. 7. (a) Particle size distribution by intensity of CP (b) particle size distribution by intensity of CPNP.

Table 3
CP particle size distribution data output.

Size Distribution	D10 [µm]	D50 [µm]	D90 [µm]	Undersize Span (D90-D10)/D50
Volume	6.432	7.802	9.162	0.350
Intensity	0.1632	5.933	8.834	1.461
Number	0.01726	0.03448	0.04858	0.908

Table 4
CPNP particle size distribution data output.

Size Distribution	D10 [nm]	D50 [nm]	D90 [nm]	Undersize Span (D90-D10)/D50
Volume	854.5	1232	1530	0.548
Intensity	594.2	952.1	1368	0.813
Number	569.1	958.2	1382	0.848

DeWaele equation ($\eta = m.\gamma^{n-1}$) at shear rate range of 1–1000 s^{-1}, whereas m is consistency index, n is flow behaviour index, γ is shear rate and η is apparent viscosity. Table 8 summarizes the fitted power law model. R^2 shows that the power law model best describes the flow of CP. A shear-thinning behavior of $n < 1$ was observed for all the solution at different concentration (Table 8).

3.5.1. Rheology of CPNF and CP solutions compared to xanthan solution

Fig. 11 shows apparent viscosity of CPNF and CP solutions compared to xanthan solution at the same concentration (2000 ppm). CPNF showed a higher viscosity compared to CP and xanthan solutions. This could be as a result of the small particle size of the CPNP. The decrease in particle size resulted in an increase in the specific surface area and available inter-particle bonding area which made the solution to be cohesive and more viscous (Adeleye et al., 2015). This agrees with prior work by Ayorinde et al. (2013) they stated that particle size and size distribution affect properties such as flowability, compaction, viscosity, emulsion, and suspension properties. It could also be because of electroviscous negative surface charge or the formation of strong particle-particle hydrogen bonds. Since the CPNP was synthesized with plant and fruit extract, carboxyl acid was deposited on the nanoparticles

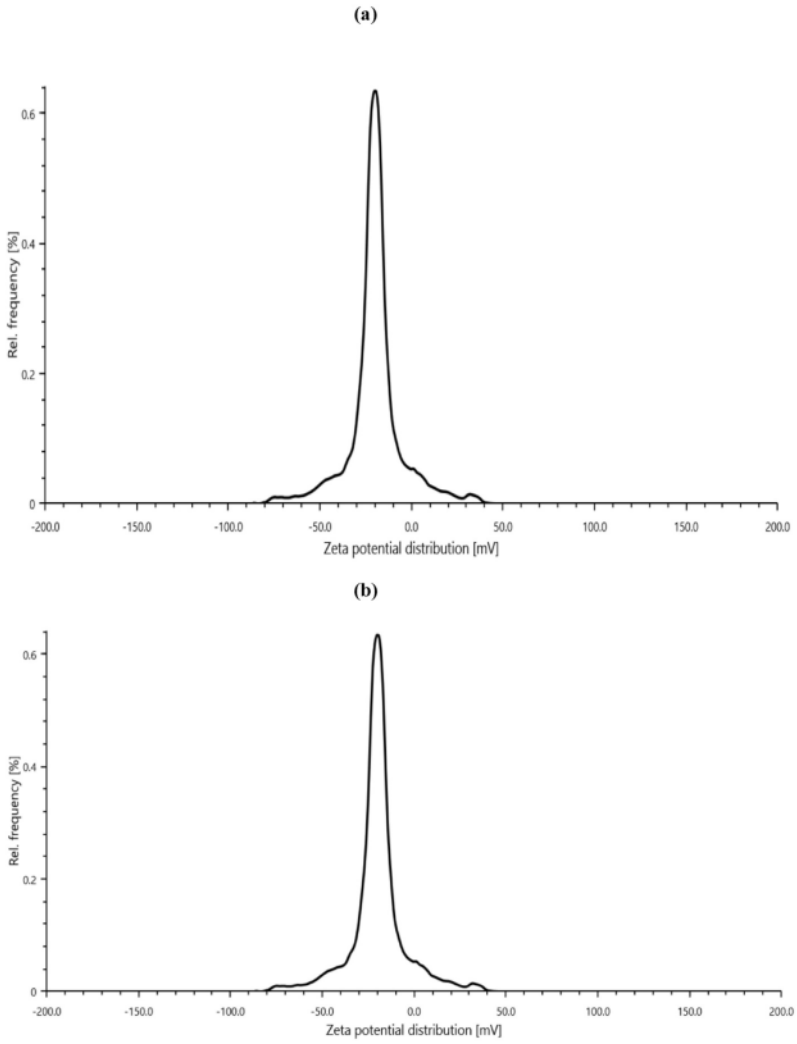

Fig. 8. (a) Zeta potential distribution of CP (b) zeta potential distribution of CPNP.

Table 5
CP zeta potential data output.

Mean Zeta Potential	−20.3 mV	Electrophoretic Mobility	−1.5790 µm*cm/Vs
Distribution Peak Value	−19.8 mV	Filter Optical Density	3.5013
Process Runs	100	Conductivity	0.077 mS/cm
Adjustable Voltage	200 V	+/− Standard Deviation	0.4 mV
Mean Intensity	366.7 kcounts/s	Transmittance	74.7%

Table 6
CPNP zeta potential data output.

Mean Zeta Potential	−25.1 mV	Electrophoretic Mobility	−1.9105 µm*cm/Vs
Distribution Peak Value	−25.1 mV	Filter Optical Density	3.7192
Process Runs	100	Conductivity	0.106 mS/cm
Adjustable Voltage	200 V	+/− Standard Deviation	0.2 mV
Mean Intensity	366.7 kcounts/s	Transmittance	72.2%

surface which imparted the negative surface charge and ionic strength in solution. This agrees with the zeta potential result (Fig. 8) and is consistent with earlier work of Shafiei-Sabet et al. (2012) they stated that the rheological properties of cellulose nanocrystals vary according to size and shape, surface charge and ionic strength. The viscosity of CP solution was higher compared xanthan solution at the same concentration (Fig. 11). This could be due to the entanglements of networks formed by the simple topological interaction of the CP chains rather than the cross-linking which might have been the case with xanthan (Adeleye et al., 2019). This is coherent with prior work of Hatscher (2016) who reported that the viscosity of schizophyllan biopolymer showed excellent resistance to shear compared to commercial polymer xanthan.

3.5.2. Viscosity of CPNF, CP and xanthan solutions as a function of electrolyte concentration

Effect of NaCl (0.9–2.2 wt%) on the apparent viscosity of CPNF was

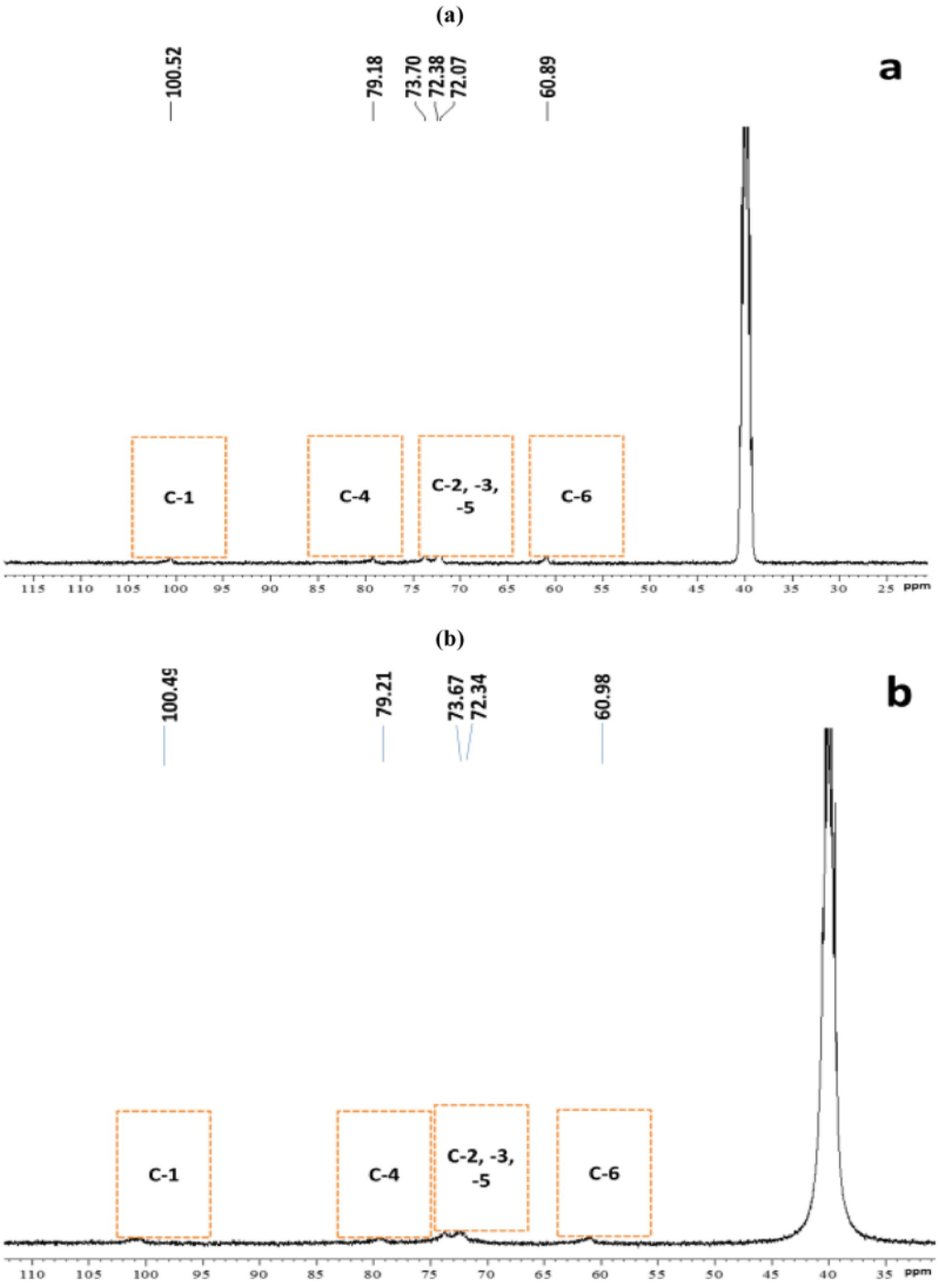

Fig. 9. ^{13}C-NMR spectra (a) CP (b) CPNP.

compared to xanthan and CP solutions at the same concentration of 2000 ppm (Fig. 12). The decrease in viscosity could be because of the change in molecular conformation as NaCl was added. The solutions without salt showed higher viscosity because of high extended molecule (Figs. 10 and 11). At low salinity concentration, NaCl imparts an electrostatic screening effect on the solutions which limited the solution expansion and declined the viscosity of the solutions (Hosseini et al., 2017). Whereas as NaCl concentration increases, negatively charged molecules of the solutions are exposed to the cations of the NaCl and are neutralized, leading to a collapse of the solutions conformation to a

Table 7
^{13}C-NMR peak assignment.

CP peak (ppm)	CPNP peak (ppm)	Assignment
100.52	100.49	C-1 carbon (CHOR)2
79.18	79.21	C-4 carbon (CH-OR)
73.70–72.07	73.6–72.34	C-2, C-3, C-5 carbon (CH–OH)
60.89	60.98	C-6 carbon (CH_2–OH)

compact coil. This result to a decline in the hydrodynamic volume of the solutions and electrostatic repulsion between the particles resulting to further decrease in viscosity. However, decrease in viscosity was less for CPNF and CP solution compared to xanthan solution (Fig. 12). This is because in the presence of water, the carboxyl group of CP increases because of its negative charge. The negative charges repelled each other leading to stretching of CP particles. The stretching resulted in increased hydrodynamic radius and viscosity in comparison to xanthan. However, when NaCl was added, the repulsion between the particles declined and the negative charge became neutral, which led to a decrease in the hydrodynamic radius and subsequently viscosity. Whereas in the case of CPNF there are two mechanism in play; the link generated by the particles will attempt to improve the viscosity while deactivation of the negative charge will seek to decrease the viscosity. At increased concentration of 2000 ppm, the impact of NaCl on the viscosity of CPNF was minimal compared to xanthan solution. Therefore, viscosity of CPNF was better compared to CP and xanthan solutions.

Table 8
m and *n* values of CP as a function of concentration.

Concentration (ppm)	Consistency Index (*m*)	Flow Index (*n*)	Stability Index (R^2)
750	0.26	0.92	0.988
1500	0.31	0.81	0.990
2000	0.37	0.49	0.999

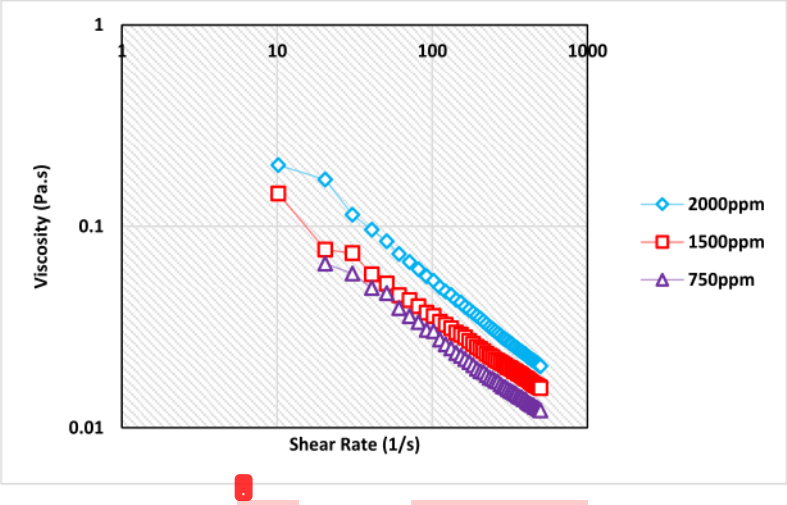

Fig. 10. Effect of concentration on apparent viscosity of CP.

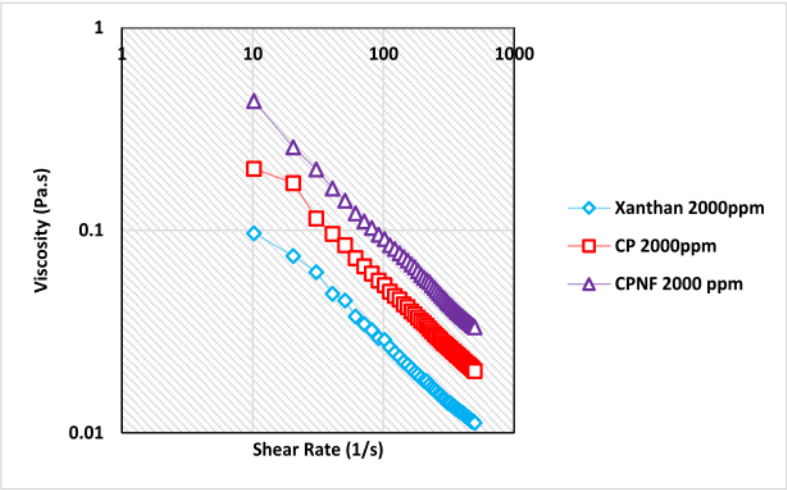

Fig. 11. Apparent viscosity of CPNF in comparison to CP and xanthan solutions.

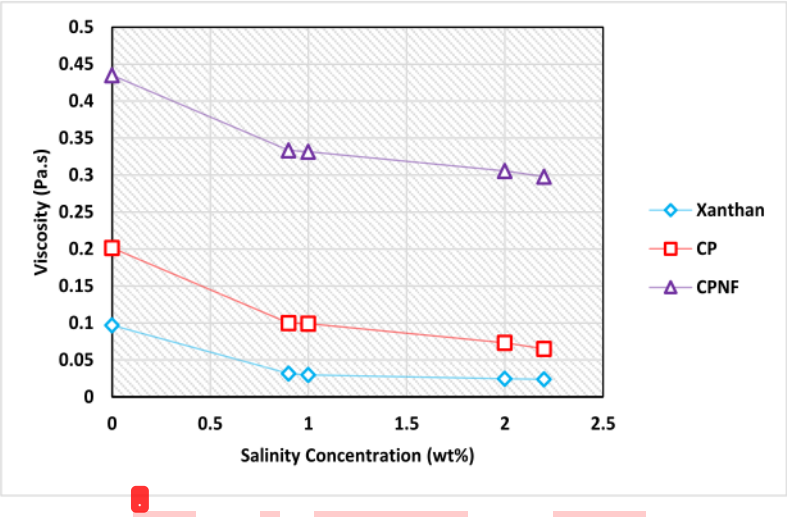

Fig. 12. Effect of salinity on the apparent viscosity of CPNF, CP, and xanthan solutions.

3.5.3. Impact of temperature on apparent viscosity of CPNF, CP and xanthan

Fig. 13 indicates that the viscosity of all the samples (CPNF, CP and Xanthan) are dependent on temperature. The viscosity of xanthan decreased as the temperature increases. This is because as the temperature increases, the mobility of the particles also increases, resulting in a decline of the intermolecular communication between the xanthan molecules. This causes coiling of the polymer macromolecules, which led to decrease in viscosity. Also, at elevated temperature, hydrogen bond amongst the xanthan molecules becomes weak. This result to a fragile link between the molecular structure and subsequently, decline in viscosity of the xanthan solution (Maurya and Mandal, 2016). Whereas, CPNF and CP solution showed a reverse trend as temperature increases from 26 to 80 °C, the viscosity increased. The result agrees with earlier work of Alakali et al. (2009) who stated that viscosity of CP solution increased as temperature increases until the boiling temperature. This might be because of the binding system of both solutions as binding increases the tensile strength and promote the formation of strong cohesive bonds between the particles (Eichie and Amalime, 2007). Before the boiling point the elements are closely bounded together, and the bonds are only broken after the boiling point. For the CPNF, the development of 3-dimensional links (micelle type) after synthesis was responsible for the increased viscosity. The formed links were still effective at elevated temperature, subsequently, leading to improved thermal stability of the CPNF than that of CP solution. The higher viscosity of CPNF compared to CP and xanthan solutions at the same concentration might be due to the packing fraction of the CPNF. The packing fraction is the measure of the degree of consolidation of the compaction (Eichie and Amalime, 2007). This implies that the CPNF might be more consolidated with closer packing of the particles than CP and xanthan solutions.

3.5.4. Influence of particle size on viscosity of CPNF

The relationship between rheology of nanofluids and particle size is important to obtain a balance in their formulation and application. The physical properties of dispersed particles such as their sizes affects the

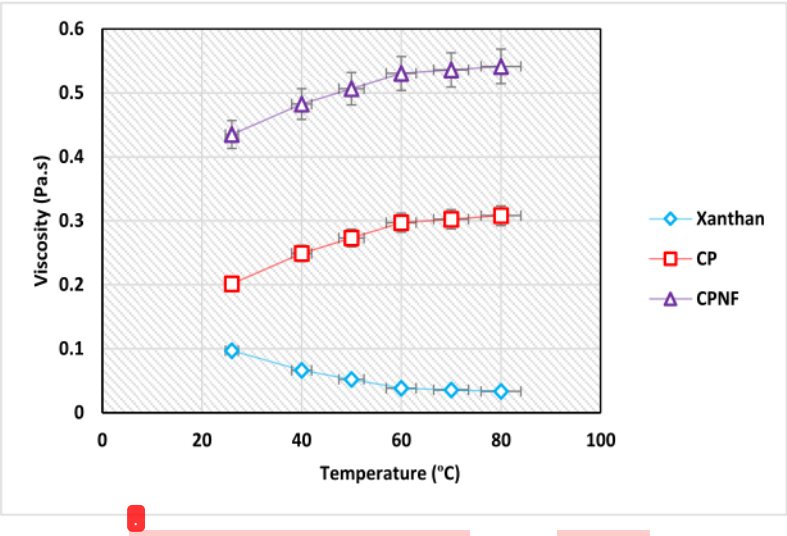

Fig. 13. Effect of temperature on apparent viscosity of CPNF, CP, and xanthan solutions.

overall characteristics of the material such as viscosity. The influence of particles sizes (10 μm, 1 μm, 100 nm and 50 nm) at the same concentration (2000 ppm) on viscosity were investigated (Fig. 14). Viscosity increased with decrease in size of the particles (Fig. 14). This is because a decrease in particles size increases the number of particles in solution and consequently, increases the probability of interaction/collision between the particles (Esfe et al., 2014; Agi et al., 2020a). The collision between the particles increases the thermal ability of the particles which is consistent with the effect of temperature on viscosity of CPNF (Fig. 13). This result was theoretically supported by Brownian motion and the liquid layering around the CPNP. Hence, the increase in particle size increases the chances of clustering and aggregation which will decrease the thermal ability of the particles as was observed with particle size 10 μm (Figs. 13 and 14).

3.6. Impact of concentration on IFT of CPNF

Impact of concentration (0.05–0.2 wt%) on the IFT of CPNF was determined. IFT declined as concentration of CPNF increased (Fig. 15). This shows that CPNF was interfacial active by reducing the IFT. Accumulation of the charged CPNF at the O/W interface might be responsible. The surface free energy was altered by the CPNF between the interface and the bulk liquid and by the electrostatic repulsive force and Van de Waals attractive force between the CPNP. CPNF reduced the IFT even at low concentration (0.05 wt%). This is because the space between the particles are larger than the size of the CPNP as such, the surface energy at the interface decreases due to repulsive force which resulted to the decrease in IFT (Ranjbar et al., 2015). Also, with increase in CPNF concentration, the particles are actively adsorbed and closely packed onto the fluid-fluid interface, which might have resulted in the reduction of the average size of the saturated oil droplets (Pal et al., 2019). CPNP replaced the O/W molecules of the initial interface therefore, the interface now is between the hydrophilic part and water on one side and hydrophobic part and oil molecules on the side of the interface. Thus, CPNF reduces the IFT due to the strong interaction compared to the earlier between dissimilar oil and water (Pillai et al., 2019). The reduction in IFT might have influenced the recovery of trapped oil.

3.6.1. Effect of electrolyte concentration on IFT of CPNF

Effect of electrolyte concentration (0.9–2.2 wt%) on the IFT of crude oil and CPNF was determined. IFT declined as concentration electrolyte increased (Fig. 16). This is because of increase in surface affinity of CPNF as a result of salting out effect. Counter-ion effect increased the packing/adsorption of CPNP at the interface. Thus, the electrolyte decreased the repulsive force between the charged CPNP. As the ionic strength increases due to salting out, the IFT decreases. It might also be due to presence of hydroxyl group from the plant extract during synthesis that increased the surface activity at the interface. This is consistent with prior work of Gaonkar (1992). They stated that the IFT decreased slightly in the presence of NaCl due to the presence of hydroxyl group in close proximity to a double bond, which affected the activity at the interface. This is consistent with the ^{13}C-NMR result in Table 7. The increase in electrolyte concentration did not inhibit IFT reduction by CPNF and no significant aggregation was observed. This could be that the steric repulsion by the adsorbed CPNF was not sensitive to electrolyte concentration. The biopolymeric chains adsorbed on the surface of CPNP provided a steric repulsive force that opposed the attractive electrolyte interaction (Phenrat et al., 2007). Similar result was observed by Tiraferri et al. (2008). They reported that no significant aggregation was observed for guar gum coated nanoparticles even at very high salt concentration 0.5 M NaCl. It might also be because of the ultrasonication, as increase in sonication time can reduce the aggregate size and prevent re-aggregation of the flocs which were broken apart during the sonication process (Tiraferri et al., 2008).

3.6.2. Effect of temperature on IFT of CPNF

Fig. 17 shows influence of temperature (26–80 °C) on IFT of CPNF (0.2 wt% w/v). The result shows that CPNF decreased IFT by 41% in comparison to NaCl (0.2 wt%) at 26 °C. This could be attributed to increase of smaller droplets. Increase in the temperature increases the number of nuclei giving rise to cavitation. Cavitation may increase due to the increase in the vapor pressure of the medium. With an increase in cavitation, the breakage of large droplet to form smaller droplet increases (Gaikwad and Pandit, 2008). It might also be as a result of higher increase in surface functional groups at the interface of CPNF compared to brine. Temperature influences IFT, entropy and free energy according to the following equations (Moeini et al., 2014; Yekeen et al., 2019).

$$\Delta G = \Delta H - T\Delta S \quad (4)$$

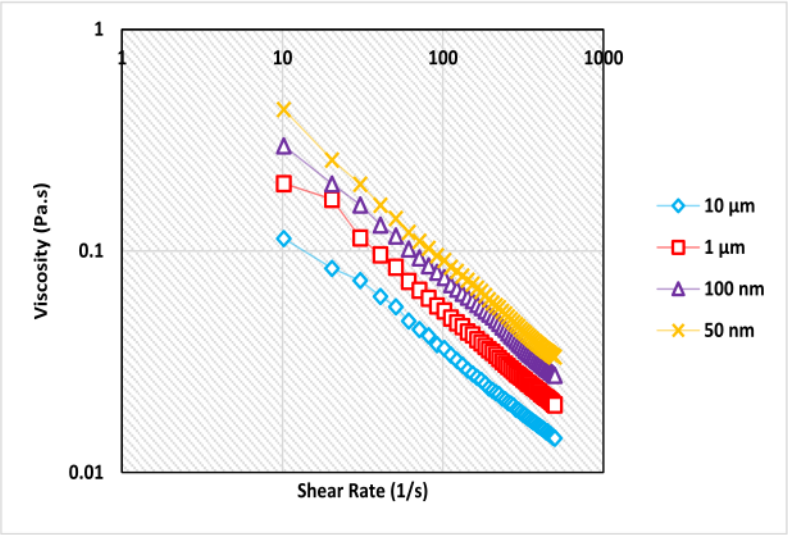

Fig. 14. Influence of particles sizes at the same concentration on viscosity.

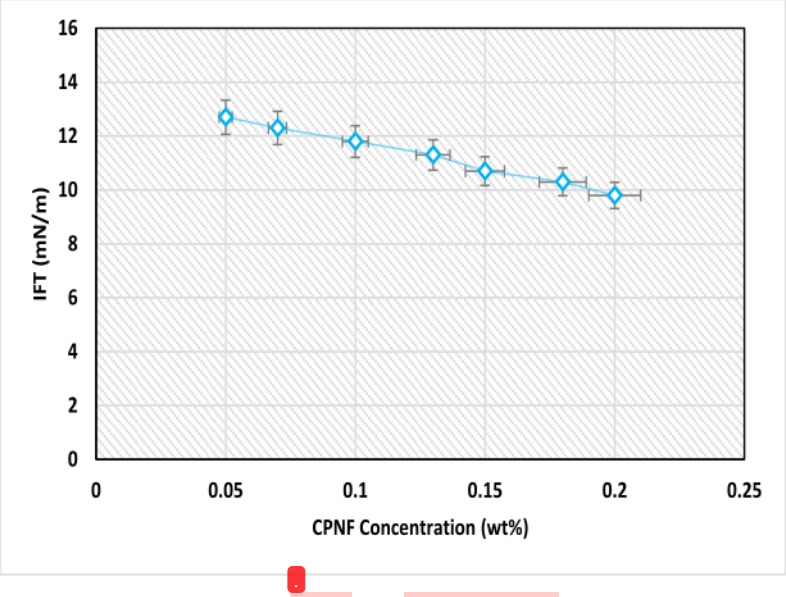

Fig. 15. Effect of CPNF concentration on IFT.

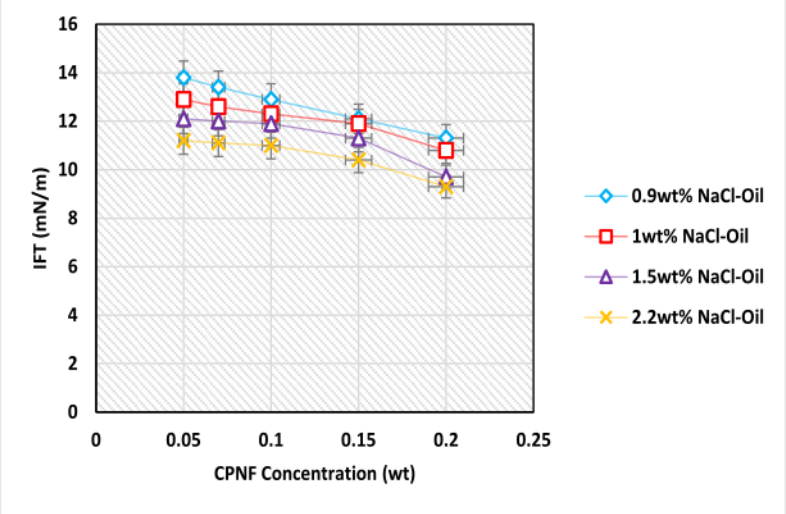

Fig. 16. Effect of NaCl concentration on IFT of CPNF.

$$\Delta G = \gamma dA \ (constant\ T\ \&\ P) \quad (5)$$

whereas ΔG is change in Gibbs free energy (kJ mol^{-1}), ΔH is change in enthalpy (kJ), ΔS is change in entropy ($J.K^{-1}$), T is temperature (K), P is pressure (Pa), γ is free energy per unit surface area of the interface between two phases (N/m). Temperature rise increased the surface-active group at fluid-fluid interfaces. This is because of increase in kinetic energy of the CPNF thereby improving the entropy. As the entropy increases, there will be a corresponding decrease in Gibbs free energy (Equation (4)). Equation (5) shows that O/W IFT reduces with increase in temperature. This is because decrease in Gibbs free energy decreases its surface free energy per unit area (Moeini et al., 2014; Yekeen et al., 2019).

3.7. Influence of CPNF on wettability alteration

Wettability plays a vital role in EOR, it controls fluid flow and distribution in porous media. The influence CPNF on wettability alteration of sandstone core was studied. Fig. 18 shows that the contact angle of CPNF-modified sandstone core decreased with increases in concentration of CPNF, which signify that the wetting ability of the sandstone core has been altered from an oil wet (125°) to water wet (30°) (Fig. 19). Ability of CPNF to change the wettability of sandstone core is governed by two mechanisms of cleaning and coating; (a) CPNF cleaned the surface of the sandstone core which led to oil removal from the surface of the sandstone core (Fig. 20a), this was due to the high affinity of the CPNF to oil molecules. (b) the cleaned surface allowed the CPNP to be

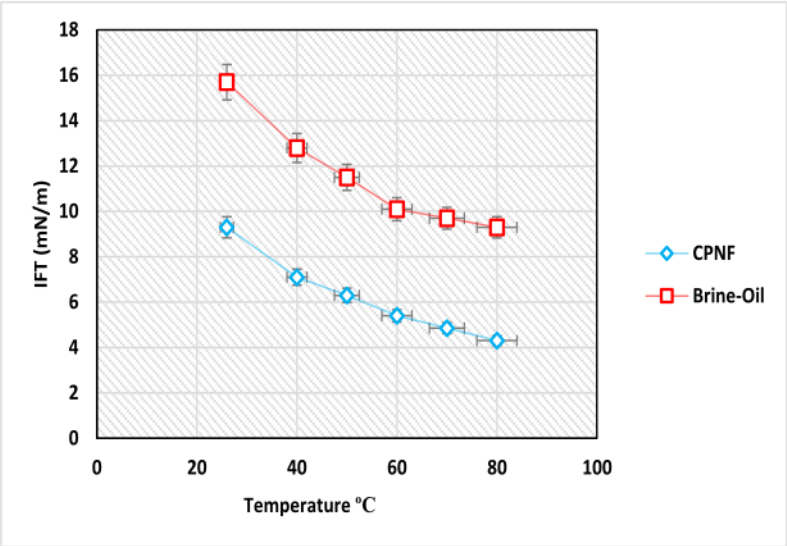

Fig. 17. Influence of temperate and electrolyte on IFT of CPNF.

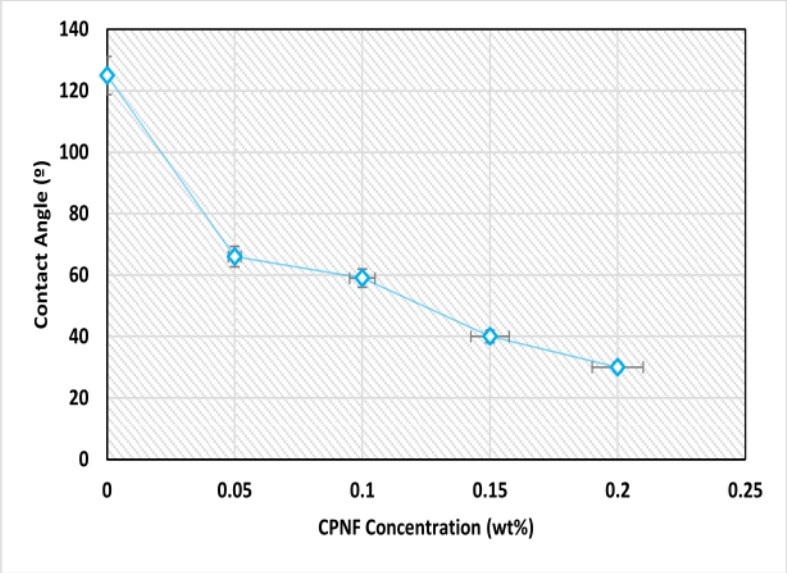

Fig. 18. Effect of CPNF concentration on wettability alteration.

coated on the surface of the sandstone core (Fig. 20 b, c, and d). Increase in concentration, increased the coating site allowing more CPNP to be coated on surface of the sandstone core which might have altered the wettability to water-wet condition (Agi et al., 2020b).

3.7.1. Influence of Electrolyte-CPNF interaction on wettability alteration

Reservoir salinities affect stability of injected nanofluid. The influence of reservoir salinities can impact the concentration of the injected nanofluid due to precipitation and adsorption of the nanofluid to the rock surface. Therefore, it is vital to investigate the effect of salinity on the contact angle of the CPNF-modified sandstone core at reservoir condition. To achieve this 0.2 wt% of CPNF dispersed in NaCl concentration (0.9–2.2 wt%) were examined. As the concentration of NaCl increased, there was a corresponding decline in angle of contact (Fig. 21). This was due to the dissociation of the two atoms of Na and Cl to form Na^+ and Cl^- ions. The Na^+ ions are attracted by the quartz in the sandstone core to form a layer. Increase in electrolyte concentration increased the positive charge of Na^+ monovalent ions on the sandstone core. Consequently, this resulted to attraction from the negative parts of polar components present in crude oil. But the monovalent ions of Na^+ covering the sandstone core prevented contact between crude oil and sandstone core. As a result of this interaction, the film present on the sandstone core surface might not be disrupted by bases or acids in the crude oil. Therefore, this was the main reason which might have altered

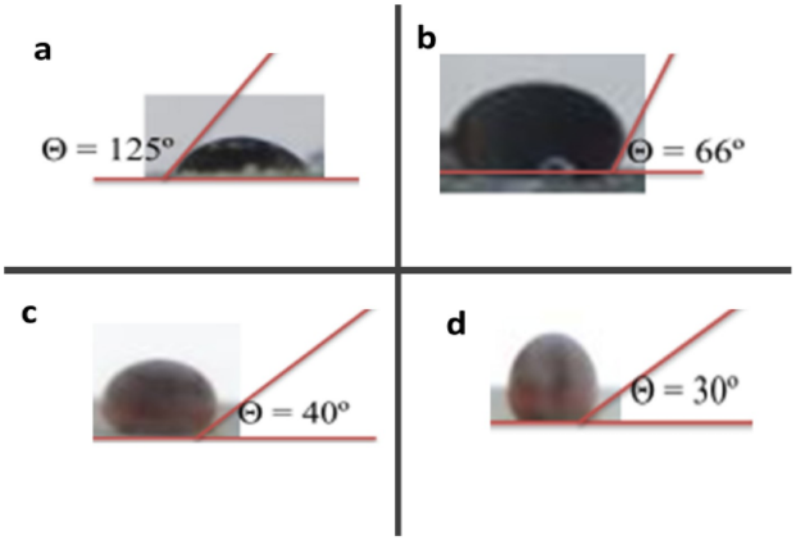

Fig. 19. Microscopic image of oil droplets (flipped image) (a) without CPNF (b) treated with 0.05 wt% of CPNF (c) 0.15 wt% of CPNF (d) 0.2 wt% of CPNF.

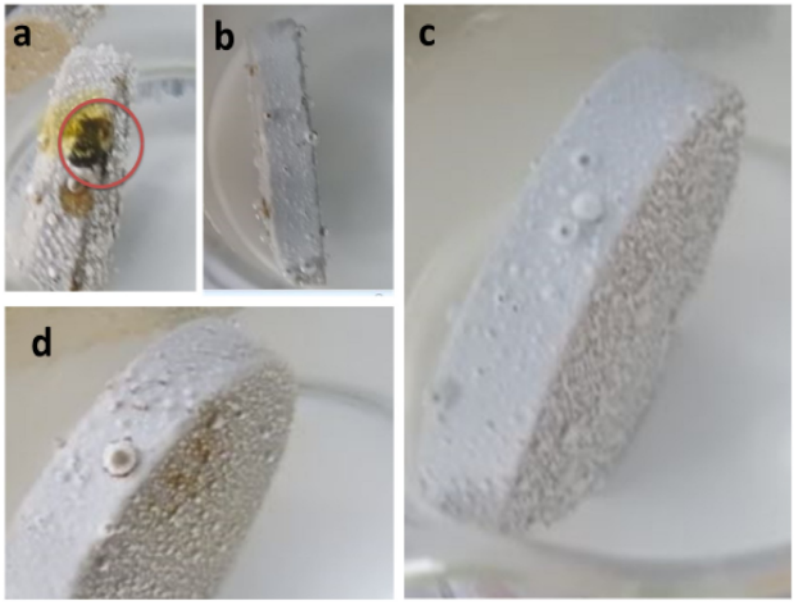

Fig. 20. (a) Oil removal (b–d) sandstone core surface coated with CPNF.

the wettability from oil-wet (116°) to water-wet (50°) as shown in Fig. 22. NaCl concentration induced a strong negative charge on the oil and brine interface (Agi et al., 2020b). This is a prove that electrokinetic charge interface of brine and oil as well as brine and rock interface may be significantly influenced by the NaCl concentration. Besides, it prevented the crude oil from spreading and adhering onto the sandstone core surface. This is because of repulsion force between brine/oil interface and brine/sandstone boundary (reactivity) as shown in Fig. 23.

3.7.2. Effect of temperature on wettability alteration

The effect of temperature on the wetting behaviour of CPNF treated sandstone was investigated. Fig. 24 shows the influence of temperature (26–80 °C) on CPNF (0.2 wt%) treated sandstone core in the presence of NaCl (2.2 wt%). Contact angle was observed to reduce as temperature increased. This is because temperature reduces the number of active sites on the sandstone core surface which influenced the spreading behaviour of the oil drop (Agi et al., 2020b). The dispersion of the CPNP front increases as temperature is increased. Temperature breaks the hydrogen bond and the water molecules desolvated the CPNP which increases the affinity of the sandstone surface towards the CPNP (Strand et al., 2006). The decline in contact angle from 110° (at 26 °C) to 16° (at 80 °C) shows that CPNF can alter the wettability of sandstone from oil-wet to water-wet (Fig. 25). As temperature increases, more CPNP was adsorbed on the sandstone surface. The mechanism is the increase in

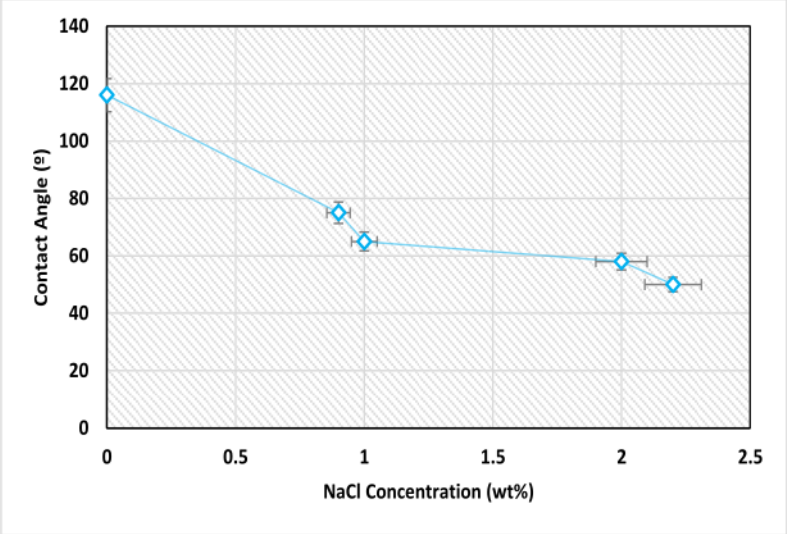

Fig. 21. Influence of electrolyte concentration on wettability alteration of CPNF-modified sandstone.

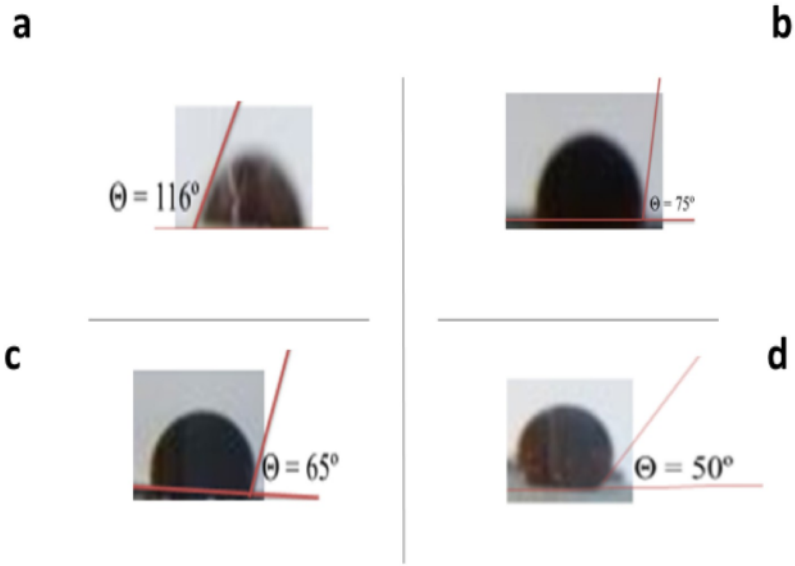

Fig. 22. Microscopic image of oil droplets (flipped image) (a) without CPNF and NaCl (b) treated with CPNF and 0.9 wt% of NaCl (c) treated with CPNF and 1 wt% of NaCl (d) treated with CPNF and 2.2 wt% of NaCl.

surface roughness of CPNP which facilitates its adhesion on the sandstone surface (Fig. 20 b-d). Also, temperature decreases asphaltenes precipitation which is washed out from the sandstone surface by the adsorbing CPNP. The nanoparticles could make asphaltene suspended in the oil and rapidly adsorb them thereby inhibiting them from being precipitated (Kazemzadeh et al., 2015). This is consistent with previous studies of Akarzadeh et al. (2004) and Escrochi et al. (2008).

3.8. Core flooding results

Core flooding experiment was conducted to determine the performance CPNF and CP solutions in comparison with commercial polymer xanthan. Cumulative oil recovery as function of injected PV is shown in Fig. 26. The oil recovery after water flooding (WF) was 48% OOIP, which implies that significant quantity of oil was bypassed in the core. EOR was started instantaneously, and CPNF improved oil recovery by 26% in comparison to 17% by CP and 11% OOIP obtained with xanthan. The higher oil recovery of CPNF and CP solutions over xanthan solution at the same concentration was due to the improved rheological properties of CPNF and CP solutions. The higher viscosities reduced the mobility of the displacing fluid and subsequently, enhanced sweep efficiency. This is coherent with flow behaviour of CPNF and CP solution (Figs. 10–13). It also shows the ability of CPNF and CP solutions to withstand high temperature condition. This agrees with prior work by

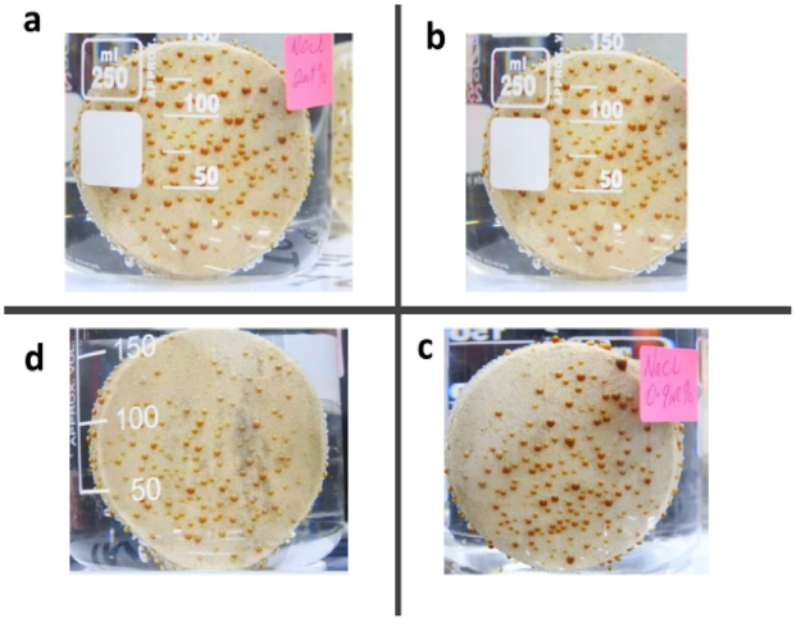

Fig. 23. Reactivity and oil expulsion.

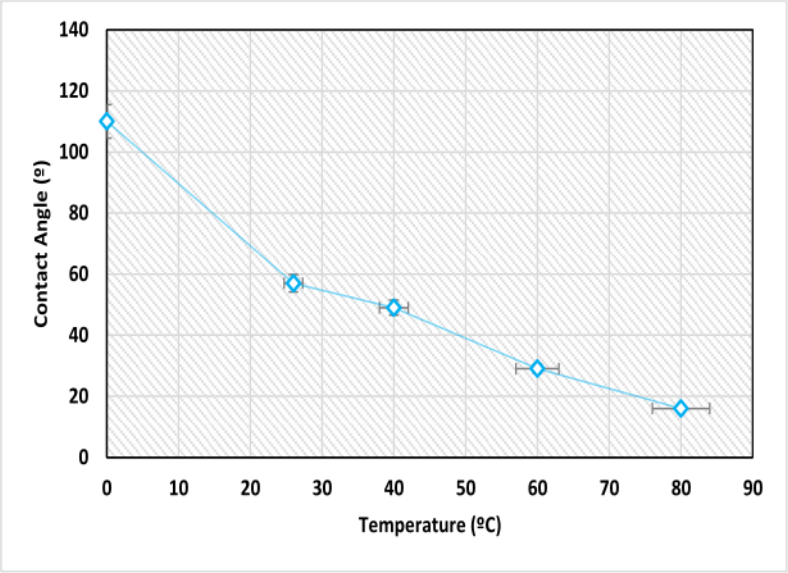

Fig. 24. Influence of temperature on wettability alteration of CPNF treated sandstone surface.

Hatscher (2016) who stated that at a temperature of 135 °C, the viscosity of schizophyllan biopolymer was still stable and the stability lasted for 300 days under anaerobic conditions. The biopolymer also exhibited superb laboratory and field pilot test results in comparison with xanthan and sulfonated polyacrylamide.

The pressure drop profile shows a good relationship with recovery result (Fig. 27). When waterflood commenced, there was a rise in pressure drops, followed by a decline until it became constant. The reason for the declining trend was due to the high mobility of water compared to oil, which was evident as BT time saw the pressure drop remain constant. EOR also led to an increase in the pressure profile, the rise during CP/xanthan flooding was due to their improved viscosity compared to water (Kumar and Mandal, 2018; Zhou et al., 2019c). A favourable type of displacement will occur if

$$\frac{k_{rw}\,\mu_w}{k_{ro}\mu_o} = M \leq 1 \tag{6}$$

whereas, M is mobility ratio, μ_o is oil viscosity (mPa.s), μ_w is water viscosity (mPa.s), k_{ro} and k_{rw} are end point relative permeabilities of oil

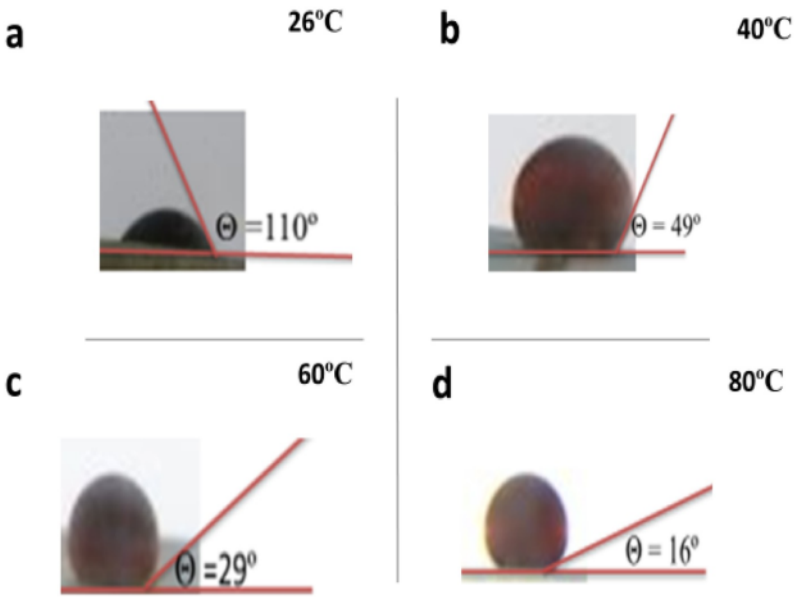

Fig. 25. Microscopic image of oil droplet (flipped image) (a) without CPNF at 26 °C (b) treated with CPNF/brine at 40 °C (c) treated with CPNF/brine at 60 °C (d) treated with CPNF/brine at 80 °C.

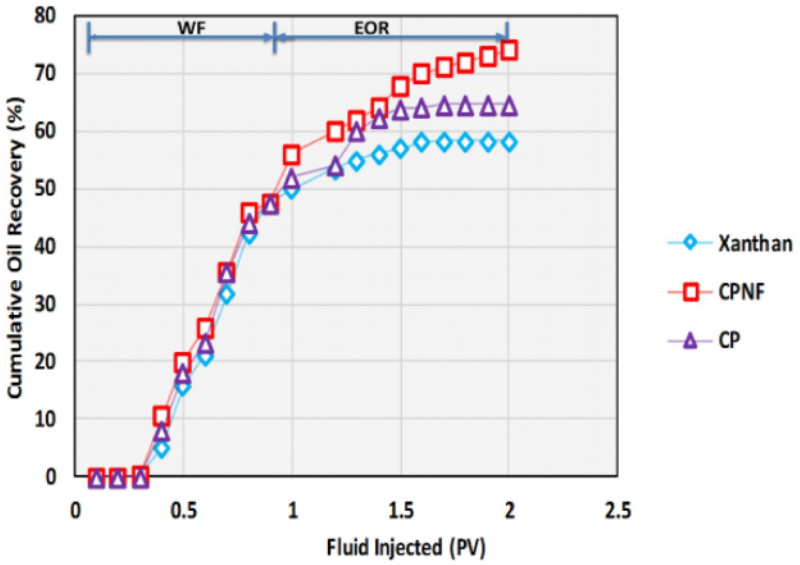

Fig. 26. Oil recovery performance of CPNF.

and water respectively (mD). Mobility ratio was determined using the method of Bamidele et al. (2009). It was observed that the mobility ratio of WF approaches unity faster than that of xanthan, CP and CPNF respectively (Fig. 28). This might have resulted in by-passing of oil and consequently early BT in the WF. The delay in approaching unity for xanthan, CP and CPNF signifies that the oil viscosity variation was less than their water viscosity variation resulting in a favourable mobility.

Recovery improved with pressure drop as CPNF was introduced. Increase in pressure drop demonstrated that CPNF lowered the capillary forces holding the oil in pore spaces (Dong et al., 2009). The pressure drops remained very high even at elevated temperature which shows that CPNF was still stable and oil displacement efficiency of CPNF was still very active at 120 °C, which resulted to increased oil recovery. As CPNF imbibe into the sandstone core to expel trapped oil, the pressure profile began to build leading to the formation of O/W emulsion (Fig. 29a). This agrees with earlier work of Pei et al. (2013) they stated that O/W emulsion enhanced the sweep efficiency by blocking the channel created by water and lowered the oil mobility. The O/W emulsion produced during CPNF injection (Fig. 29a) can be correlated with the coating formed during sandstone core treatment with CPNF (Fig. 20 b-d). This singular trend might be responsible for the improved recovery, as the coating detached the oil out of the core and additional

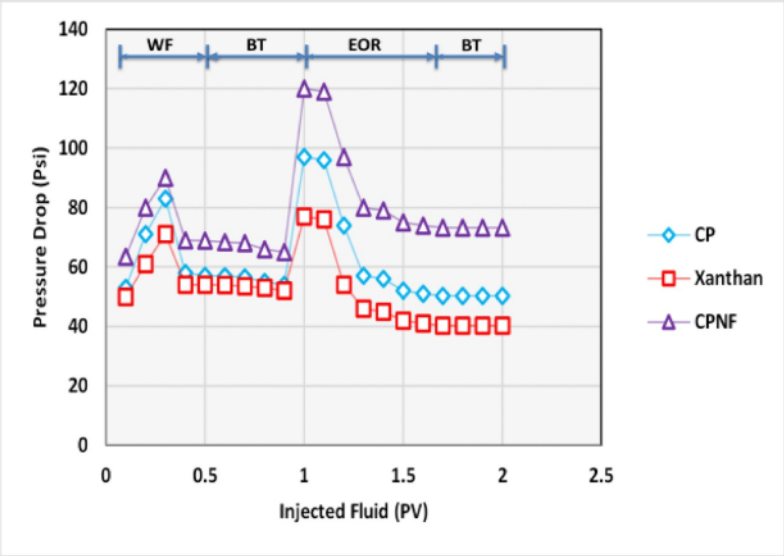

Fig. 27. Pressure drop trend of CPNF.

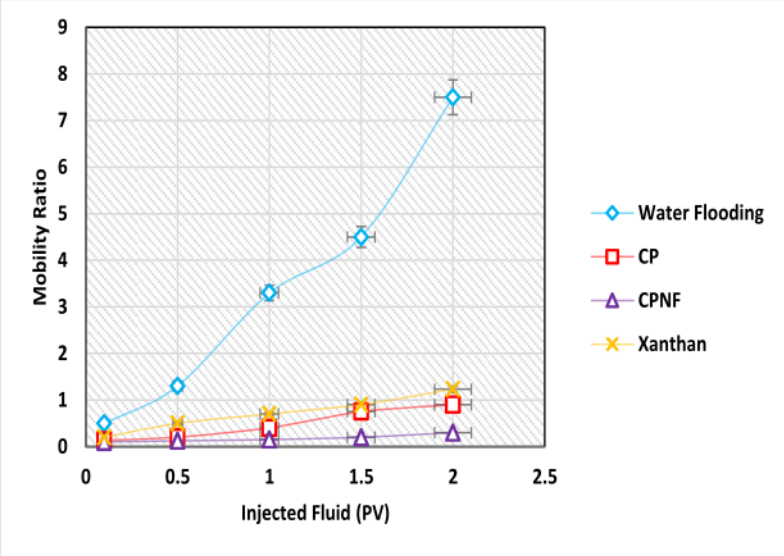

Fig. 28. Mobility ratio of injected fluids.

oil was expelled. However, this was not the case in CP and xanthan injection as emulsion was not produced (Fig. 29b). The emulsion generated was examined with an Amscope microscope (Fig. 30). The emulsion has small diameter droplets which signifies stability of the emulsion.

3.9. Effects of CPNF on capillary forces

(i) Capillary Number, Nc: capillary number is a dimensionless parameter used to analyse fluid flow. It is the ratio of the viscous forces to the IFT. It provides information on fluid flow inside the core before and after injection of CPNF. Wettability alteration of the oil-wet sandstone core to water-wet can be observed qualitatively through the capillary number. Fig. 31 shows the effect of CPNF on capillary number. It was observed that increase in concentration of CPNF increased capillary number. This implies that the viscous forces are dominant over capillary forces (Faiyas et al., 2017). CPNF had a higher capillary number compared to brine. This is because of lower IFT of CPNF compared to brine, which was coherent with IFT results and proves that capillary number was dependent on IFT. The upsurge in capillary number signifies that capillary forces has decreased, and flow of oil has increased through the pores. It can be said that increases in capillary number improved the pore scale displacement efficiency of CPNF.

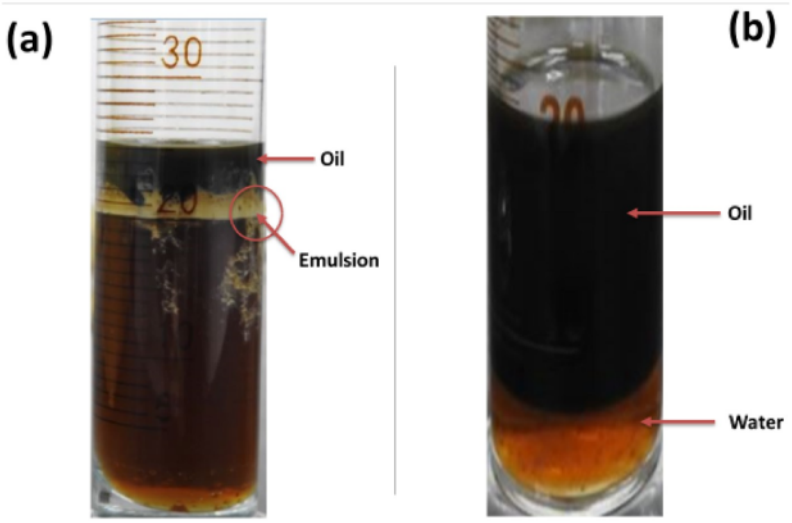

Fig. 29. (a) O/W emulsion during CPNF injection (b) CP and xanthan injection no O/W emulsion.

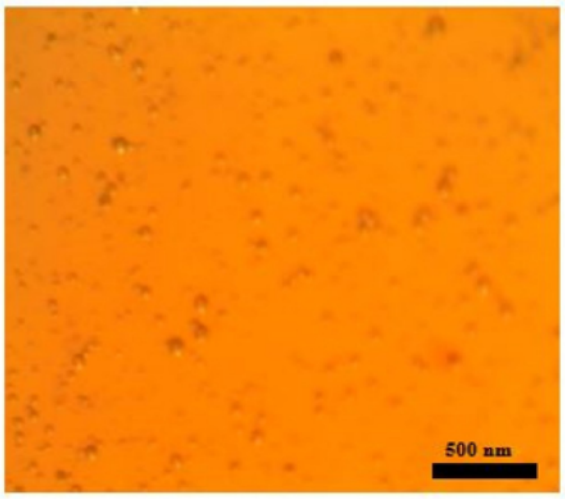

Fig. 30. Microscopic image of emulsion generated from CPNF Flooding.

(ii) Bond Number, N_B: Bond number is the ratio of gravitational forces to IFT. It measures the importance of IFT compared to gravitational forces. Fig. 32 shows the effect of CPNF on Bond number, the increase in CPNF concentration increased the Bond number (Fig. 32). This implies that increase in bond number improved the concentration of the CPNF compared to brine. This is because increase in Bond number reduced the dimensionless value of the CPNP deposited on the pore surface and the dimensionless volume concentration of the CPNP entrapped on the pore throats (El-Amin et al., 2015). The intermediary values of the Bond number (Fig. 32) indicates a non-trivial balance between the forces. This agrees with prior work of El-Amin et al. (2015) they stated that a higher Bond number indicate that the system was relatively unchanged by the IFT, whereas a lesser Bond number (less than 1) indicates that the IFT controls the system.

The results were validated with previous study of Franklin (1994) using the equation:

$$S_{or} = 0.02 + 0.0505 \log\left(\frac{0.01227}{N_c + 0.5N_B}\right) \quad (7)$$

whereas S_{or} is dimensionless residual oil saturation, N_c and N_B are capillary number and Bond number, respectively. It shows that there is a correlation between IFT, S_{or}, capillary number and Bond number (Fig. 33). As the IFT decreases the residual oil saturation decreases, the capillary and Bond number increases. This shows a transition from capillary dominated flow to gravity dominated flow as IFT reduces, which accounts for this observation (Schechter et al., 1994). The remaining oil in the porous media can be displaced by an increased viscous force, which pushes the oil out or by a reduced capillary force which holds the oil in the porous media (Nobakht et al., 2007).

4. Energy utilized and cost estimation

The energy used for this work was estimated as 3×10^4 J/g which is three times lesser than the amount needed for steam explosion (9.90×10^4) and other traditional approaches (Adewuyi and Deshmane, 2015; Velmurugan and Muthukumar, 2012). Similar result was reported by earlier work of Nitayavardhana et al. (2010) they stated that the energy utilization for ultrasound production of ethanol from synthesis of cassava was twice lesser (11 kJ) than heat synthesis (22 kJ). Also, this is consistent with prior work of Bubalo et al. (2013) and Mullick and Neogi (2018). They stated that ultrasound synthesis is easier, saves time and energy utilization is 45–65% and 96% less than traditional techniques. About US$ 1,114,447/year can be saved if a company invest in ultrasonic synthesis rather than traditional techniques (Montalbo-Lomboy et al., 2011). Approximately US$229/year was utilized in the purchase of equipment and raw materials for this work. This amount was 25% lesser compared to the price of producing photoelectrochemical (PEC) nanoparticles (James et al., 2009). To augment this laboratory process to commercial scale, it will require the same energy per unit volume to get a similar result if ultrasound was used with the same formulation (Hielscher, 2005; Lionelli and Mason, 2010). CPNP can be manufactured in commercial scale by converting traditional ultrasound horn to the half-wave Barbell Horn (Peshkovsky and Bystryak, 2014). The manufacturing capability can rise by a factor of about $2(D_{hbh}/D_{ch})^2$ (where D_{ch} and D_{hbh} are output tip diameters of the two horns), that is,

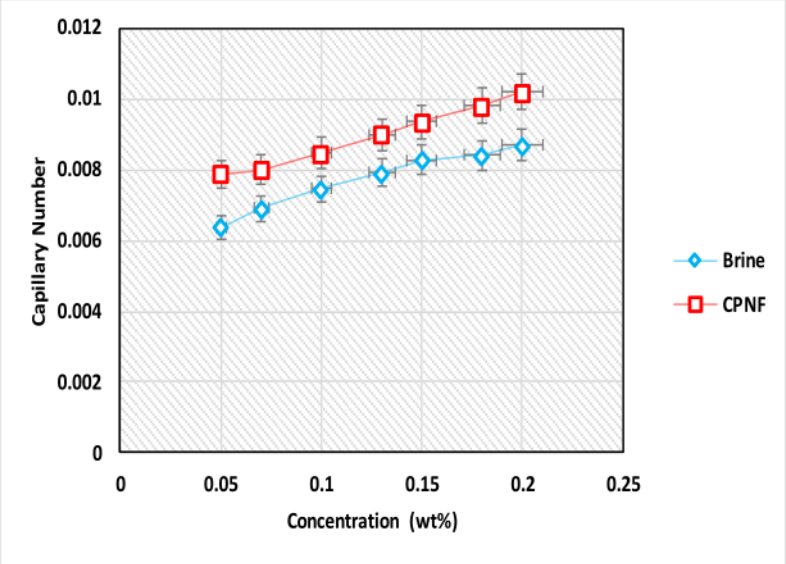

Fig. 31. Effect of CPNF on capillary number.

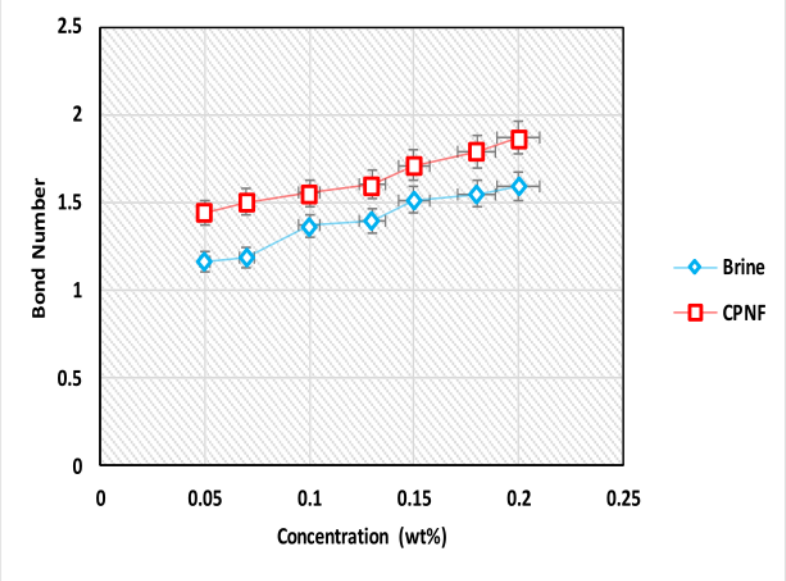

Fig. 32. Effect of CPNF on Bond number.

scale-up factor of 50–60 using this approach. Therefore, high amplitude ultrasonic wave can be transmitted from laboratory to large scale manufacturing (Lionelli and Mason, 2010; Peshkovsky and Bystrak, 2014). The low energy utilization, low investment and operation cost and the use of low-cost products such as CP (US$ 0.15/kg); oranges (US$ 0.56/kg); pineapple (US$ 0.75/kg) and palm wine (US$ 0.1/litre) makes this approach a good comparison to other methods.

5. Conclusions

In this study, CP natural polymer was formulated and synthesized to form CPNP for EOR purpose. The physical properties of the CP and CPNP including their size distribution were investigated by TEM and DLS. The influence of the process variables was studied. It was discovered that the type of nanoparticles formed depends on the extraction methods and influence of process intensification. The rheological properties of the CPNF was compared with CP natural polymer and commercial polymer xanthan. From the experimental results, the concentration, the particle morphology, and the surface charge of the solutions were the contributing factors that influenced the rheology of the system. The CPNF, CP and xanthan aqueous solutions exhibited shear-thinning and pseudo-plastic behavior. The R^2 value for the model was very close to unity,

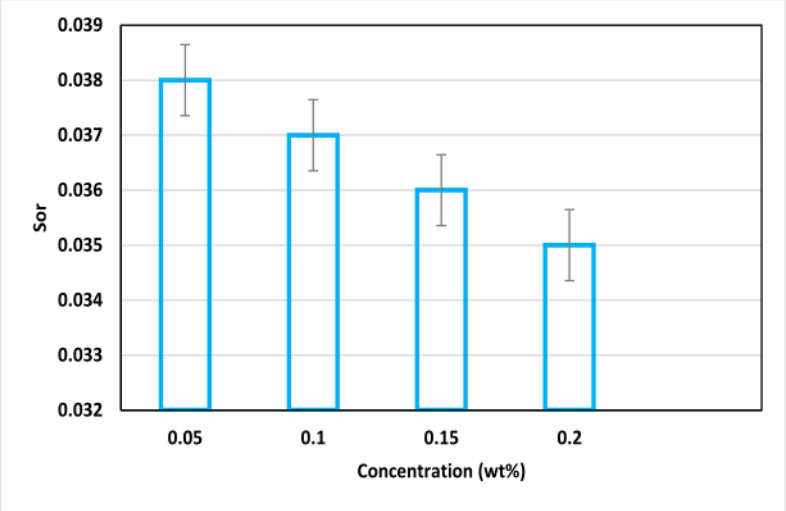

Fig. 33. Effect of capillary and Bond number on dimensionless residual oil saturation.

which indicated that the power law model best described the rheological behavior. The consistency index increased as the flow behavior indexes decreased with increase in the concentration. The interfacial properties and the wettability alteration efficiency of the CPNF was investigated at different concentration and temperatures. The IFT decreased with increase in concentration, electrolyte, and temperature. The results showed that CPNF could change the wettability of sandstone at low concentration, high salinity, and elevated temperature. To justify the finding highlighted above, the CPNF and CP natural polymers were applied for EOR purposes at reservoir condition. The CPNF were very effective in mobilizing residual oil at HTHP reservoir condition. Experimental results revealed that there was a correlation between IFT, S_{or}, capillary number and Bond number. The energy consumption and cost estimation demonstrated that the method and polymeric nanofluid were cost-effective compared to other methods and products.

Declaration of competing interest

The authors have no conflict of interest.

CRediT authorship contribution statement

Augustine Agi: Conceptualization, Methodology, Formal analysis, Investigation, Data curation, Writing - original draft, Visualization. **Radzuan Junin:** Conceptualization, Methodology, Validation, Resources, Visualization, Supervision, Funding acquisition. **Mohammed Omar Abdullah:** Methodology, Validation, Resources, Visualization, Supervision. **Mohd Zaidi Jaafar:** Methodology, Validation, Resources, Visualization, Supervision, Funding acquisition. **Agus Arsad:** Methodology, Validation, Resources, Supervision, Funding acquisition. **Wan Rosli Wan Sulaiman:** Methodology, Validation, Resources, Supervision. **M.N.A. Mohd Norddin:** Methodology, Resources. **Muslim Abdurrahman:** Software, Validation, Formal analysis, Data curation, Project administration. **Azza Abbas:** Software, Validation, Formal analysis, Data curation. **Afeez Gbadamosi:** Formal analysis, Investigation, Data curation. **Nur Bashirah Azli:** Investigation, Resources, Project administration.

Acknowledgment

The authors would like to thank the Ministry of Higher Education (MOHE), Malaysia and Universiti Teknologi Malaysia for supporting this research through Research Management Grant Vot. No. R. J130000.7846.4F946, UTM-TDR43.1, and TDR43.2.

Appendix A. Supplementary data

Supplementary data to this article can be found online at https://doi.org/10.1016/j.petrol.2020.107476.

References

Abbas, A., Moslemizadeh, A., Sulaiman, W.R., Jaafar, M.Z., Agi, A., 2020. An insight into di-chain surfactant adsorption onto sandstone minerals under different salinity-temperature conditions: chemical EOR applications. Chem. Eng. Res. Des. 153, 657–665.

Adeleye, O., Oyewo, M., Odeniyi, M., 2015. Physicochemical and rheological characteristics of Cissus populnea gum extracted by different solvent. West Afr. J. Pharmacy 26 (1), 113–126.

Adeleye, O.A., Femi-Oyewo, M.N., Odeniyi, M.A., Ajala, T.O., 2019. Evaluation of Cissus populnea gum as a directly compressible matrix system for tramadol hydrochloride extended-release tablet. J. Appl. Pharmaceut. Sci. 9 (2), 105–111.

Adewuyi, Y.G., Deshmane, V., 2015. Intensification of enzymatic hydrolysis of cellulose using high-frequency ultrasound: an investigation of the effects of process parameters on glucose yield. Energy Fuels 29, 4998–5006.

Agi, A., Junin, R., Gbadamosi, A., 2018a. Mechanism governing nanoparticles flow behaviour in porous media: insight for enhanced oil recovery applications. Int. Nano Lett. 8 (2), 49–77.

Agi, A., Junin, R., Gbonhinbor, J., Onyekonwu, M., 2018b. Natural polymer flow behaviour in porous media for enhanced oil recovery applications: a review. J. Petrol. Explor. Prod. Technol. https://doi.org/10.1007/s13202-018-0434-7.

Agi, A., Junin, R., Chong, A.S., 2018c. Intermittent ultrasonic wave to improve oil recovery. J. Petrol. Sci. Eng. 166, 577–591.

Agi, A., Junin, R., Gbadamosi, A., Abbas, A., Azli, N.B., Oseh, J., 2019a. Influence of nanoprecipitation on crystalline starch nanoparticle formed by ultrasonic assisted weak-acid hydrolysis of cassava starch and the rheology of their solutions. Chem. Eng. Processing-Process Intensification 142, 107556.

Agi, A., Junin, R., Abbas, A., Gbadamosi, A., Azli, N.B., 2019b. Influence of ultrasonic on the flow behaviour and disperse phase of cellulose nanoparticles at fluid- fluid interface. Nat. Resour. Res. 1–20.

Agi, A., Junin, R., Alqatta, A.Y.M., Gbadamosi, A., Yahya, A., Abbas, A., 2019c. Ultrasonic ultrafiltration process for the emulsification of oil field produced water treatment. Ultrason. Sonochem. 51, 214–222.

Agi, A., Junin, R., Arsad, A., Abbas, A., Gbadamosi, A., Azli, N.B., Oseh, J., 2019d. Synergy of the flow behaviour and disperse phase of cellulose nanoparticles in enhancing oil recovery at reservoir condition. PloS One 14, 9. https://doi.org/10.1371/journal.pone.0220778.

Agi, A., Junin, R., Arsad, A., Abbas, A., Gbadamosi, A., Azli, N.B., Oseh, J., 2020a. Ultrasonic-assisted weak-acid hydrolysis of crystalline starch nanoparticles for chemical enhanced oil recovery. Int. J. Biol. Macromol. 148, 1251–1271.

Agi, A., Junin, R., Abbas, A., Gbadamosi, A., Azli, N.B., 2020b. Effect of dynamic spreading and the disperse phase of crystalline starch nanoparticles in enhancing oil

recovery at reservoir condition of a typical Sarawak oil field. Appl. Nanosci. 10 (1), 263–279.
Akarzadeh, K., Sabbagh, O., Beck, J., Svrcek, W.Y., Yarranton, H.W., 2004. Asphaltene precipitation from bitumen diluted with n-alkanes. In: Paper PETSOC-2004-026-EA, Presented at Canadian International Petroleum Conference Held in Calgary, Alberta, 8-14 June.
Alakali, S.J., Irtwange, V.S., Mkavga, M., 2009. Rheological characteristics of food gum (Cissus populnea)'. Afr. J. Food Sci. 3 (9), 237–242.
Awonorin, S.A., 1993. Rheological and Mechanical Properties of B-Vitamin Retention and Sensory Characteristics of Sausage Made from Broiler Chicken and Guinea Fowl, vol. 20. Lebensmittal-Wess-U-Technol, pp. 291–300.
Ayorinde, J.O., Itiola, O.A., Odeniyi, M.A., 2013. Effect of excipients and formulation types on the compressional of diclofenac. Acta Poloniae-Drug Res. 70 (3), 557–566.
Baalousha, M., Lead, J.R., 2013. Nanoparticle dispersity in toxicology. Nat. Nanotechnol. 8, 308–309.
Bamidele, A., Fadairo, A., Falode, A., 2009. Endpoint mobility ratios for vertical and horizontal wells with incidence of scale deposition. Open Petrol. Eng. J. 2, 17–23.
Bel Haaj, S., Magnin, A., Petrier, C., Boufi, S., 2013. Starch nanoparticles formation via high power ultrasonication. Carbohydr. Polym. 92, 1625–1632.
Bouatay, F., Meksi, N., Slah, F., Fm, M., 2014. Chemical modification of cellulosic fibres using eco-friendly compounds to improve dyeing with cationic dyes. J. Textil. Sci. Eng. 42 (2), 4–11.
Brar, V., Kaur, G., 2018. Preparation and characterisation of polyelectrolyte complexes of Hibiscus esculenta (Okra) gum and chitosan. Int. J. Biomater. https://doi.org/10.1155/2018/4856287.
Bubalo, M.C., Sabotin, I., Rados, I., Valentincic, J., Bosiljkov, T., Brncic, M., Znidarsic-Plazl, P., 2013. A comparative study of ultrasound, microwave, and microreactor-assisted imidazolium-based ionic liquid synthesis. Green Process. Synth. 2, 579–590.
Cano-Sarmiento, C., Tellez-Medina, D.I., Viveros-Contreras, R., Cornejo-Mazon, M., Figueroa-Hernandez, C.Y., Garcia-Armenta, E., Alamilla-Beltran, L., Garcia, H.S., Gutierrez-Lopez, G.F., 2018. Zeta potential of food matrices. Food Eng. Rev. https://doi.org/10.1007/s12393-018-9176-z.
Chin, S., Pang, S., Tay, S., 2011. Size controlled synthesis of starch nanoparticles by a simple nanoprecipitation method. Carbohydr. Polym. 86, 1817–1819.
Chuah, A.M., Kuroiwa, T., Ichikawa, S., Kobayashi, I., Nakajima, M., 2009. formation of biocompartible nanoparticles via the self-assembly of chitosan and modified lecithin. J. Food Sci. 74 (1), 1–8.
Cofrades, S., Antoniou, I., Solas, M.T., Herrero, A.M., Jimenez-Colmenero, F., 2013. Preparation and impact of multiple (Water-in-Oil-in-Water) emulsion in meat systems. Food Chem. 141, 338–346.
David-Birman, T., Mackie, A., Lesmes, U., 2013. Impact of dietary fibers on the properties and proteolytic digestibility of lactoferrin nano-particles. Food Hydrocolloids 31 (1), 33–41.
Deshmukh, A.S., Aminabhavi, T.M., 2015. Pharmaceutical application of various natural gums. In: Ramawat, K.G., Merillon, J. (Eds.), Polysaccharides, Bioactivity and Biotechnology. Springer International Publishing, Switzerland, pp. 1933–1968.
Dong, M., Ma, S., Liu, Q., 2009. Enhanced heavy oil recovery through interfacial instability: a study of chemical flooding for brintnell heavy oil. Fuel 88, 1049–1056.
Dufresne, A., 2008. Cellulose-Based Composites and Nanocomposites. Monomers, Polymers, Composites from Renewable Resources, pp. 401–418.
Eichie, F.E., Amalime, A.E., 2007. Evaluation of the binder effects of the gum of mucilages of Cissus populnea and acassia Senegal on the mechanical properties of paracetamol tablets'. Afr. J. Biotechnol. 6 (19), 2208–2211.
El-Amin, M.F., Salama, A., Sun, S., 2015. Numerical and dimensional analysis of nanoparticles transport with two-phase flow in porous media. J. Petrol. Sci. Eng. 128, 53–64.
Escrochi, M., Nabipour, M., Ayatollahi, S., Mehranbod, N., 2008. Wettability alteration at elevated temperature: consequences of asphaltene precipitation. Louisiana, USA. In: Paper SPE-112428-MS, Presented at SPE International Symposium and Exhibition on Formation Damage Control Held in Lafayette, pp. 13–15 (February).
Esfe, M.H., Saedodin, S., Mahian, O., Wongwises, S., 2014. Efficiency of ferromagnetic nanoparticles suspended in ethylene glycol for application in energy devices: effects of particle sizes, temperature and concentration. Int. Commun. Heat Mass Tran. 58, 138–146.
Faiyas, A., Erich, S., Huinink, H., Adan, O., 2017. Transport of a water-soluble polymer during drying of a model porous media'. Dry. Technol. 35 (15), 1874–1886.
Franklin, M.J., 1994. Scale-up for Miscible Flood Process for Heterogenous Reservoirs. Petroleum Engineering Department, Stanford University, Stanford, California, USA.
Gaikwad, S., Pandit, A., 2008. Ultrasound emulsification: effect of ultrasound and physiochemical properties on dispersed phase volume and droplet size. Ultrason. Sonochem. 15, 554–563.
Gaonkar, A.G., 1992. Effects of salt, temperature, and surfactants on the interfacial tension behavior of a vegetable oil/water system. J. Colloid Interface Sci. 149 (1), 256–260.
Gbadamosi, A.O., Kiwalabye, J., Junin, R., Manan Augustine, A., 2018. A review of gas enhanced oil recovery schemes used in the North Sea. J. Petrol. Explor. Prod. Technol. 8, 1373–1387, 04.
Gbadamosi, A., Junin, R., Manan, M., Agi, A., Oseh, J., 2019a. Nanotechnology Application in Chemical Enhanced Oil Recovery: Current Opinion and Recent Advances. Intechopen, pp. pp1–23.
Gbadamosi, A., Junin, R., Manan, M., Agi, A., Oseh, J., Usman, J., 2019b. Synergistic application of aluminium oxide nanoparticles and oilfield polyacrylamide for enhanced oil recovery. J. Petrol. Sci. Eng. 182, 106345.
Gbadamosi, A., Junin, R., Manan, M., Agi, A., Oseh, J., Usman, J., 2019c. Effect of aluminium oxide nanoparticles on oilfield polyacrylamide: rheology, interfacial tension, wettability and oil displacement studies. J. Mol. Liq. 296, 111863.
Gbadamosi, A.O., Junin, R., Manan, M.A., Yekeen, N., Agi, A., 2020. Hybrid suspension of polymer and nanoparticles for enhance oil recovery. Polym. Bull. 76, 6193–6230.
Goncalves, P., Norena, C., Silveira, N., Brandelli, A., 2014. Characterization of starch nanoparticles obtained from acraucaria angustifolia seeds by acid hydrolysis and ultrasound. LWT- Food Sci. Technol. 58, 21–27.
Goyal, R., Macri, L.K., Kaplan, H.M., Kohn, J., 2016. Nanoparticles and nanofibers for topical drug delivery. J. Contr. Release 240, 77–92.
Guidelli, E.J., Ramos, A.P., Zaniquelli, M.E., Baffa, O., 2011. Green synthesis of colloidal silver nanoparticles using natural rubber latex extracted from Hevea brasiliensis. Spectrochim. Acta: Mol. Biomol. Spectrosc. 82, 140–145.
Hatscher, S., 2016. Schizophyllan as a Biopolymer for EOR Lab and Field Results. Winterfall, International Energy Agency (IEA), Germany.
Hielscher, T., 2005. Ultrasonic Production of Nano-Size Dispersion and Emulsions. ENS, pp. 138–143.
Hosseini, E., Mozafari, H.R., Hojjatoleslamy, M., Rousta, E., 2017. Influence of temperature, pH and salts on the rheological properties of bitter almond gum. Food Sci. Technol. 37 (3), 437–443.
James, B., Baum, G., Perez, J., Baum, K., 2009. Technoeconomic Analysis of Photoelectrochemical (PEC) Hydrogen Production. Directed Technologies, Arlington, Virginia, USA.
Kalesi, H., Emadzadeh, B., Kadkhodace, R., Fang, Y., 2016. Whey protein isolate-Persian gum interaction at neutral pH. Food Hydrocolloids 59, 45–49.
Kazemzadeh, Y., Eshranghi, S., Kazemi, K., Sourani, S., Mehrabi, M., Ahmadi, Y., 2015. Behavior of asphaltene adsorption onto the metal oxide nanoparticles surface and its effect on the heavy oil recovery. Ind. Eng. Chem. Res. 54 (1), 233–239.
Kim, H., Park, D., Kim, J., Lim, S., 2013. Preparation of crystalline starch nanoparticles using cold acid hydrolysis and ultrasonication. Carbohydr. Polym. 98, 295–301.
Ku, B.K., Maynard, A.D., 2005. Comparing aerosol surface-area measurement of monodisperse ultrafine silver agglomerates by mobility analysis, transmission electron microscopy and diffusion charging. J. Aerosol Sci. 36, 1108–1124.
Kumar, N., Mandal, A., 2018. Surfactant stabilized oil-in-water nanoemulsion: stability, interfacial tension and rheology study for enhanced oil recovery application. Energy Fuels 32 (6), 6452–6466.
LeCorre, D., Bras, J., Dufresne, A., 2010. Starch nanoparticles: a review. Biomacromolecules 11, 1139–1153.
LeCorre, D., Bras, J., Dufresne, A., 2011. Evidence of micro- and nanoscaled particles during starch nanocrystals preparation and their isolation. Biomacromolecules 12, 3039–3046.
Lionelli, C., Mason, T.J., 2010. Microwave and ultrasonic processing: now a realistic option for industry. In: Chemical Engineering and Processing: Process Intensification, pp. 885–900.
Luzi, F., Fortunati, E., Puglia, D., Lavorgna, M., Santulli, C., Kenny, J., Torre, J., 2014. Optimized extraction of cellulose nanocrystals from pristine and carded hemp fibres. Ind. Crop. Prod. 56, 175–186.
Maurya, N.K., Mandal, A., 2016. Studies on the behaviour of suspension of silica nanoparticles in aqueous polyacrylamide solution for application in enhanced oil recovery. Petrol. Sci. Technol. 34 (5), 429436.
Moeini, F., Hemmati-Sarahpardeh, A., Ghazanfari, M.-H., Masihi, M., Ayatollahi, S., 2014. Towards mechanistic understanding of heavy crude oil/brine interfacial tension: the role of salinity, temperature and pressure. Fluid Phase Equil. 375, 191–200.
Montalbo-Lomboy, M., Khanal, S.K., Van Leeuwen, J.H., Raj Raman, D., Grewell, D., 2011. Simultaneous saccharification and fermentation and economic evaluation of ultrasonic and jet cooking pre-treatment of corn slurry. Biotechnol. Prog. 27, 1561–1569.
Moon, R., Martini, A., Nairn, J., Simonsen, J., Youngblood, J., 2011. Cellulose nanomaterial review: structure, properties and nanocomposites. Chem. Soc. Rev. 7 (40), 3941–3994.
Mullick, A., Neogi, S., 2018. Acoustic cavitation induced synthesis of zirconium impregnated activated carbon for effective fluoride scavenging from water by adsorption. Ultrason. Sonochem. 45, 65–77.
Nitayavardhana, S., Shrestha, P., Rasmussen, M., Lamsal, B.P., Van Leeuwen, J.H., Khanal, S.K., 2010. Ultrasound improved ethanol fermentation from cassava chips in cassava based ethanol plants. Bioresour. Technol. 101, 2741–2747.
Nobakht, M., Moghadam, S., Gu, Y., 2007. Effects of viscous and capillary forces on CO2 enhanced oil recovery under reservoir conditions. Energy Fuel. 21, 3469–3476.
Okachi, H., Nakano, M., 2000. Preparation and evaluation of W/O/W. Type emulsion containing vancomycin. Adv. Drug Deliv. Rev. 45, 5–26.
Oladimeji, A.T., Okechukwu, D.O., 2016. Modified food gum (Cissus populnea) fibers: microstructural behaviour, physico-mechanical properties and kinetics of water adsorption. J. Eng. Appl. Sci. 11 (17), 10655–10663.
Pal, N., Kumar, N., Mandal, A., 2019. Stabilization of dispersed oil droplets in nanoemulsions by synergistic effects of the gemini surfactant, PHPA polymer, and silica nanoparticle. Langmuir 35, 2655–2667.
Pei, H., Zhang, G., Ge, J., Jin, I., Ma, C., 2013. Potential of alkaline flooding to enhance heavy oil recovery through water-in oil emulsion'. Fuel 104, 272–278.
Peshkovsky, A., Bystryak, S., 2014. Continuous-flow production of a pharmaceutical nanoemulsion by high-amplitude ultrasound: process scale-up. Chem. Eng. Process: Process Intensification 82, 132–136.
Phenrat, T., Saleh, N., Sirk, K., Tilton, R., Lowry, G., 2007. Aggregation and sedimentation of aqueous nanoscale zerovalent iron dispersions. Environ. Sci. Technol. 41 (1), 284–290.
Pillai, P., Saw, R., Singh, R., Padmanabhan, E., Mandal, A., 2019. Effect of synthesized lysine-grafted silica nanoparticle on surfactant stabilized O/W emulsion stability: application in enhanced oil recovery. J. Petrol. Sci. Eng. 177, 861–871.

Pope, G.A., 2011. Recent developments and remaining challenges of enhanced oil recovery'. J. Petrol. Technol. 63, 65–68, 07.
Ranjbar, H., Khosravi-Nikou, M., Safiri, A., Bovard, S., Khazaei, A., 2015. Experimental and theoretical investigation on nano-fluid surface tension. J. Nat. Gas Sci. Eng. 27, 1806–1813.
Schechter, D.S., Zhou, D., Orr Jr., F.M., 1994. Low IFT drainage and imbibition. J. Petrol. Sci. Eng. 11 (4), 283–300.
Scott, B.C., Healliwll, J.B., Aruoma, O.B., 1993. Evaluation of the antioxidant actions of ferulic acid and catechins. Free Radic. Res. Commun. 19 (4), 241–253.
Shafiei-Sabet, S., Hamad, W.Y., Hatzikiriakos, S., 2012. Rheology of nano-crystalline cellulose aqueous suspensions. Langmuir 28 (49), 17124–171333.
Shahrodin, N.S., Rahmat, A.R., Arsad, A., 2015. Synthesis and characterisation of cassava starch nanocrystals by hydrolysis method. Adv. Mater. Res. 1113, 446–452.
Strand, S., Hognesen, E.J., Austad, T., 2006. Wettability alteration of carbonates-effects of potential determining ions (Ca2+ and SO42-) and temperature. Colloid. Surface. Physicochem. Eng. Aspect. 275, 1–10.
Suslick, K.S., 2001. Sonoluminescence and sonochemistry. In: Meyers, R.A. (Ed.), Enyclopedia of Physical Science and Technology. Academic, San Diego.
Suslick, K.S., Eddingsaas, N., Flanningan, D., Hopkins, S., Xu, H., 2018. The chemical history of a bubble. Acc. Chem. Res. 51 (9), 2169–2178.
Tiraferri, A., Chen, K., Sethi, R., Elimelech, M., 2008. Reduced aggregation and sedimentation of zero-valent iron nanoparticles in the presence of guar gum. J. Colloid Interface Sci. 324, 71–79.
Velmurugan, R., Muthukumar, K., 2012. Sono-Assisted enzymatic saccharification of sugarcane bagasse for bioethanol production. Biochem. Eng. J. 63, 1–9.
Wei, C., Xu, B., Qin, F., Yu, H., Chen, C., Meng, X., Zhu, L., Wang, Y., Gu, M., Liu, Q., 2010. C-type starch from high-amylose rice resistant starch granules modified by antisense RNA inhibition of starch branching enzyme. J. Agric. Food Chem. 58, 7383–7388.
Yekeen, N., Padmanabhan, E., Idris, A.K., 2019. Synergetic effect of nanoparticles and surfactant on n-decane-water interfacial tension and bulk foam stability at high temperature. J. Petrol. Sci. Eng. 179, 814–830.
Yildirim, M., Sumnu, G., Sahin, S., 2016. Rheology, particle-size distribution, and stability of low-fat mayonnaise produced via double emulsion. Food Sci. Biotechnol. 25 (6), 1613–1618.
Zasoski, R.J., 2008. In: Chesworth, W. (Ed.), Encyclopaedia of Soil Science. Springer, Netherlands.
Zetasizer Nano Series User Manual, 2015. Malvern Instruments, MAN0317(2.2).
Zhou, M., Xia, L., He, Y., Zhang, L., Qiao, X., Zhong, X., 2015a. Synthesis of new salt-resistant sulfonate gemini surfactants with hydroxyl groups. J. Surfactants Deterg. 18 (2), 303–308.
Zhou, M., Wang, C., Xing, T., Li, S., Zhang, Z., Luo, G., 2015b. Studies on foam flooding for saline reservoirs after polymer flooding. J. Petrol. Sci. Eng. 135, 410–420.
Zhou, M., Nie, X., Zhou, L., Hou, L., Zhao, J., Yang, Y., 2017. Study of crosslinked copolymer nanospheres with temperature resistance, salinity resistance, and deep profile control. J. Appl. Polym. Sci. 134 (40), 45131.
Zhou, M., Bu, J., Ma, Y., Zhou, J., Fu, H., Yang, F., 2018a. Synthesis of new sulfobetaine gemini surfactants with hydroxyls and their effects on surface-active properties. J. Surfactants Deterg. 21 (6), 867–877.
Zhou, M., Bu, J., Wang, J., Guo, J., Huang, J., Huang, M., 2018b. Study on three phase foam for Enhanced Oil Recovery in extra-low permeability reservoirs. Oil Gas Sci. Technol. Rev. IFP Energies Nouvelles 73, 55.
Zhou, M., Zou, J., Guo, X., Yang, Y., 2019a. Superabsorbent nanocomposite and its properties. J. Macromol. Sci., Pure Appl. Chem. 56 (5), 496–505.
Zhou, M., Zou, J., Gu, Y., Yi, R., Tu, H., 2019b. Preparation of magnetic polymer nanosphere and its profile control. J. Dispersion Sci. Technol. https://doi.org/10.1080/01932691.2019.1593860.
Zhou, M., Yi, R., Gu, R., Tu, H., 2019c. Synthesis and evaluation of a Tetra-copolymer for oil displacement. J. Petrol. Sci. Eng. 179, 669–674.

DrEngMuslim - Karya Ilmiah - Application Of Polymeric Nanofluid In Enhancing Oil Recovery At Reservoir Condition

ORIGINALITY REPORT

20%	15%	18%	3%
SIMILARITY INDEX	INTERNET SOURCES	PUBLICATIONS	STUDENT PAPERS

MATCH ALL SOURCES (ONLY SELECTED SOURCE PRINTED)

9%

★ Augustine Agi, Radzuan Junin, Agus Arsad, Azza Abbas, Afeez Gbadamosi, Nur Bashirah Azli, Jeffrey Oseh. "Synergy of the flow behaviour and disperse phase of cellulose nanoparticles in enhancing oil recovery at reservoir condition", PLOS ONE, 2019

Publication

Exclude quotes	On	Exclude matches	< 1%
Exclude bibliography	On		